

CHAPTER 12

III-Nitride-Based UV Photodetectors

E. MONROY¹, F. CALLE¹, E. MUÑOZ¹ and F. OMNÈS²

¹*Dpto. Ingeniería Electrónica, ETSI Telecomunicación,
Universidad Politécnica de Madrid, Ciudad Universitaria,
28040-Madrid, Spain*

²*Centre pur le Recherche sur l'Heteroepitaxie et
ses Applications (CNRS), Parc Sophia Antipolis,
Rue Bernard Gregory, 06560-Valbonne, France*

12.1	INTRODUCTION	527
12.2	PHOTODETECTOR PARAMETERS	530
12.2.1	Responsivity, Gain, and Quantum Efficiency	530
12.2.2	UV/Visible Contrast	531
12.2.3	Bandwidth and Time Response	531
12.2.4	Noise Equivalent Power	532
12.2.5	Detectivity	532
12.3	III-NITRIDE PHOTOCONDUCTORS	533
12.3.1	General Principles	533
<i>12.3.1.1</i>	<i>Responsivity</i>	534
<i>12.3.1.2</i>	<i>Time response</i>	535
<i>12.3.1.3</i>	<i>Noise</i>	536
12.3.2	Responsivity	537
<i>12.3.2.1</i>	<i>Variation with incident power and temperature</i>	537
<i>12.3.2.2</i>	<i>Spectral response</i>	538
<i>12.3.2.3</i>	<i>Responsivity models</i>	538
12.3.3	Time Response	543
<i>12.3.3.1</i>	<i>Experimental results</i>	543
<i>12.3.3.2</i>	<i>Mid-gap trap</i>	545

<i>12.3.3.3 Metastable (DX-like) defects</i>	546
<i>12.3.3.4 Modulation of the conduction section</i>	547
12.3.4 Frequency Response	550
12.3.5 Noise	552
12.3.6 Photoconductors on Insulating GaN	553
12.4 SCHOTTKY PHOTODIODES	553
12.4.1 General Principles	554
<i>12.4.1.1 Responsivity</i>	554
<i>12.4.1.2 Time response</i>	555
<i>12.4.1.3 Noise</i>	555
12.4.2 Device Structures and Responsivity	556
<i>12.4.2.1 Backside illumination</i>	556
<i>12.4.2.2 Frontside illumination, vertical structure</i>	557
<i>12.4.2.3 Frontside illumination, planar structure</i>	557
12.4.3 Time Response	560
12.4.4 Noise Performance	560
12.4.5 Schottky Photodiodes on ELOG GaN	562
12.4.6 Schottky Photodiode as Biological UV Sensor	564
12.4.7 Schottky Photodiode Arrays	564
12.5 METAL-SEMICONDUCTOR-METAL (MSM) PHOTODIODES	565
12.5.1 General Principles	565
<i>12.5.1.1 Band diagram</i>	566
<i>12.5.1.2 Responsivity</i>	567
<i>12.5.1.3 Time response</i>	568
12.5.2 Current-Voltage Characteristic	569
12.5.3 Responsivity	570
<i>12.5.3.1 Linearity and spectral response</i>	570
<i>12.5.3.2 Bias dependence</i>	572
12.5.4 Time Response	574
12.5.5 Noise Performance	574
12.5.6 MSM Photodiodes on ELOG GaN	575
12.6 p-n AND p-i-n PHOTODIODES	575
12.6.1 General Principles	575
<i>12.6.1.1 Responsivity</i>	575
<i>12.6.1.2 Time response</i>	576
<i>12.6.1.3 Noise</i>	577
12.6.2 Responsivity	578
12.6.3 Time Response	580
12.6.4 Noise	580
12.6.5 p-i-n Photodiodes on ELOG GaN	582
12.6.6 GaN-Based Avalanche Photodiodes	583

12.7 PHOTOTRANSISTORS	584
12.7.1 Bipolar Phototransistors	584
12.7.2 Field Effect Phototransistors	585
12.8 CONCLUSIONS	585
Acknowledgments	587
References	587

12.1 INTRODUCTION

The ultraviolet (UV) region of the electromagnetic spectrum covers the wavelengths between 400 nm (3.1 eV) and 10 nm (124 eV),¹ and it is conventionally divided into three bands:

- UV-A, from 400 to 320 nm (3.1–3.87 eV)
- UV-B, from 320 to 280 nm (3.87–4.43 eV)
- UV-C, from 280 to 10 nm (4.43–124 eV)

This highly ionizing radiation is able to activate a number of chemical processes. The most important natural UV source is the Sun. Solar UV radiation corresponds to 9 percent of the total energy outside the Earth's atmosphere.² However, the stratospheric ozone layer prevents radiation with wavelengths shorter than 280 nm to reach the Earth's surface, and the UV radiation remaining can be further attenuated due to contamination in the low troposphere.³

In the recent years, the study of the depletion of the stratospheric ozone layer, and thus the reduction of its capability to filter UV-B and UV-C radiations, is a scientific priority that has promoted the development of UV sensors for environmental monitoring. In addition, UV photodetectors present a wide range of applications. Because they are able to identify flames in a hot background, they can be used in fire alarms, missile plume detection, or combustion monitoring systems. Medical applications, such as sterilization or detection of biological and chemical agents, have also been proposed. Their use in communication systems is especially interesting for intersatellite communications, because wavelengths below 280 nm cannot be interfered from Earth. Also, the use of UV light in optical data storage systems, such as compact discs, would make possible to multiply their present capacity four-fold. Finally, stable and accurate UV detectors are necessary for calibration of UV sources and for astronomical and astrophysical studies.

Traditionally, UV detection has been accomplished by photomultiplier tubes (PMTs), thermal detectors, and narrow-bandgap semiconductor photodiodes. PMTs exhibit high gain and low noise, and can be fairly visible-blind. However, they are expensive, large, physically fragile instruments, requiring

high power supplies, and they are susceptible to magnetic fields. Thermal detectors (pyrometers and bolometers) generally are used for calibration in the UV range. Although they are useful as radiometric standards, these detectors are slow and their response is wavelength independent.

Semiconductor photodetectors are small, lightweight, insensitive to magnetic fields, and they do not require high voltage sources. Their low cost, good linearity and sensibility, and capability for high-speed operation make semiconductor devices an excellent approach for UV detection. There are different kinds of semiconductor photodetectors: photoconductors, Schottky barrier photodiodes, metal-semiconductor-metal (MSM) photodiodes, p-n and p-i-n photodiodes, and field effect and bipolar phototransistors.⁴ The structures of these devices is depicted in Figure 12.1.

Different semiconductors have been applied to UV detection. Table 12.1 compares relevant properties of these materials. Due to its well-established technology, silicon (Si) is the semiconductor most commonly used for UV photodiodes, although commercial GaAs- and GaAsP-based photodiodes are also available. The main problem for these narrow-bandgap semiconductor devices is device aging, due to absorption of radiation with energy much higher than the semiconductor bandgap. On the other hand, visible and infrared blindness is often required. The use of wide-bandgap semiconductors (i.e., diamond, SiC, III-nitrides, wide-bandgap II-VI materials) makes it possible to avoid filters and reduces aging effects. Moreover, wide-bandgap materials are chemically and thermally more stable, which is an advantage for some UV-detector applications requiring operation in harsh environments.

III-nitrides (i.e., AlN, GaN, InN, and their ternary compounds) present some advantages over other wide-bandgap semiconductors: high absorption

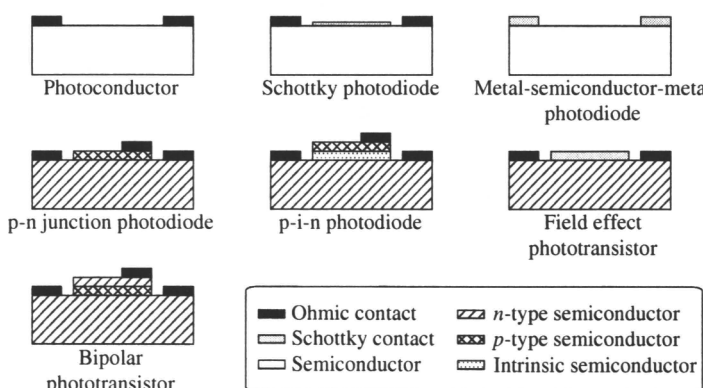


Figure 12.1 Schematic structure of different semiconductor photodetectors

Table 12.1 Basic parameters of semiconductors applied to UV photodetectors

	<i>Si</i>	<i>GaAs</i>	<i>GaP</i>	<i>3C-SiC</i>	<i>4H-SiC</i>	<i>6H-SiC</i>	<i>GaN</i>	<i>AlN</i>	<i>InN</i>	<i>C</i>
E_G (eV)	1.12	1.43 direct	2.26	2.39	3.2	2.86	3.39 direct	6.2 direct	1.89 direct	5.5
Thermal conductivity ($\text{W cm}^{-1} \text{K}^{-1}$)	1.5	0.5	1.1	3.2	4.9	4.9	1.3	3.19	0.8	20
Melting point (K)	1690	1510	1740	3100	3100	3100	2791	3487	2143	4370
Electron saturation velocity (10^7 cm/s)	1	2	1.25		2	2	2.5	1.4	2.5	2.7
Mobility (cm^2/Vs)										
electrons	1400	8500	350	1000	950	400	1250	300	3200	2200
holes	600	400	100	50	120	75	850	14		1600
Dielectric constant	11.8	12.5	11.1	9.7	9.7	9.7	9	8.5	15.3	5.5
Breakdown field (10^5 V/cm)	3	6	10	20	20	24	26	20		100

coefficients and sharper cutoffs, due to their direct bandgap; the possibility of selecting the cutoff wavelength by changing the mole fraction of their ternary alloys; and their capability for heterojunction devices.

Regarding high-speed operation, III-nitrides present several potential advantages over other compound semiconductors. The high breakdown field should make possible reduced downscaling limits, with concomitant improvements in the frequency response of transit-time-limited devices. The saturation velocity for GaN is also higher than that of GaAs, and the optical phonon energies are about threefold greater. This can be quite beneficial for transient transport, because it would delay the onset of optical phonon emission. By using shorter transit lengths and low temperatures to suppress phonon absorption, the delayed onset could be utilized to achieve and maintain ballistic transport.

With all these advantages, III-nitrides have become the most promising materials for the fabrication of optoelectronic devices (both emitters and detectors) in the blue and UV regions of the spectrum.⁵

In this chapter, we first define the most important parameters that characterize semiconductor photodetectors. Then, different III-nitride based photodetector devices are treated in separate sections, including a theoretical introduction to their general principles, a review of the evolution and state-of-the-art of these detectors, compiling their main features (responsivity, time response, noise), and discussing the models proposed to explain their performance.

12.2 PHOTODETECTOR PARAMETERS

The most important parameters that characterize the performance of semiconductor photodetectors are: responsivity, gain, quantum efficiency, contrast, bandwidth, noise equivalent power, and detectivity.^{4,6,7}

12.2.1 Responsivity, Gain, and Quantum Efficiency

The *current responsivity* of the detector, R_i , is defined as the photogenerated current, I_{ph} , per unit of incident optical power, P_{opt} :

$$R_i = \frac{I_{ph}}{P_{opt}} (\text{A/W}) \quad (12.1)$$

The responsivity is determined by the quantum efficiency, η , and by the photoelectric gain, g . *Quantum efficiency* is the number of electron–hole pairs generated per incident photon; its value describes the quality of the coupling between the detector and the radiation. *Gain* is the number of carriers detected per photogenerated electron–hole pair, and it gives an idea

of the efficiency of the carrier collection system. Taking these parameters into account, the current responsivity for a certain wavelength, λ , is given by:

$$R_i = q \frac{\lambda}{hc} \eta g \quad (12.2)$$

where q is the electron charge, h is Planck's constant and, c is the speed of light.

12.2.2 UV/Visible Contrast

For some applications, it is important that the photodetector response presents a sharp cutoff at a certain wavelength, λ_{cutoff} . The *UV/visible contrast*, or visible rejection ratio, is often used to evaluate the sharpness of the cutoff, and it can be defined as the ratio between the responsivity at the cutoff wavelength and the responsivity at 400 nm:

$$\text{UV/VIS} = \frac{R_i(\lambda_{cutoff})}{R_i(\lambda = 400 \text{ nm})} \quad (12.3)$$

12.2.3 Bandwidth and Time Response

The photodetector speed can be limited by capacitive effects, by carrier trapping, or by the saturation velocity of carriers in the semiconductor. All these phenomena contribute to reduce of the responsivity at high frequencies. The *photodetector bandwidth* is defined as the frequency at which the responsivity has dropped to half its value at low frequencies, and it is expressed in Hz.

In the time domain, the device shows a finite time response, which is characterized by the decay time, τ_d , (or rise time, τ_r), defined as the time in which the photocurrent drops from 90 percent to 10 percent (or increases from 10 percent to 90 percent) of its maximum value, when the device is excited with rectangular light pulses.

In the special case of exponential transient response, the decay time and the rise time are related to the exponential time constant, τ , and to the bandwidth, BW, by the expressions:

$$\text{BW} = \frac{1}{2\pi\tau} = \frac{2.20}{2\pi\tau_d} = \frac{2.20}{2\pi\tau_r} \quad (12.4)$$

It is very important to notice that information about the bandwidth can only be obtained from the rise time only if the excitation pulse is rectangular, with a rise time much shorter than τ_r , and a pulse width much larger than τ_r , so that photocurrent increases from zero to a steady-state value.

12.2.4 Noise Equivalent Power

In semiconductor devices, there are five main sources of noise⁸:

- *Shot noise*, due to the random emission of carriers crossing potential barriers.
- *Thermal (Johnson) noise*, due to random collisions of carriers with the lattice.
- *Partition noise*, due to the division of the current in two flows toward different contacts.
- *Generation-recombination noise*, due to the generation and recombination of carriers, either band-to-band or through trap levels.
- *1/f (flicker) noise*, characterized by a $1/f^\gamma$ spectrum with $\gamma \propto 1$, and related to the presence of traps in contacts, at the surface or within the semiconductor, as well as to leakage currents and to superficial defects. No general theory exists that satisfactorily explains this sort of noise. The most accepted models are Hooge's model,⁹ which attributes the noise to fluctuations in the free carrier mobility, and McWhortel's model,⁸ which attributes the noise to fluctuations in the free carrier density.

The *noise equivalent power* (NEP) is the optical power required to generate a photocurrent equal to the noise level. For a photodetector with a responsivity R_i , the NEP is given by:

$$\text{NEP} = \frac{I_n}{R_i} (\text{W}) \quad (12.5)$$

where I_n is the root mean square (rms) value of the noise current.

In the case of white noise, NEP increases with the square root of the detector bandwidth. Thus, to evaluate the noise performance of a detector, it is more convenient to give the NEP normalized for frequency bandwidth:

$$\text{NEP}^* = \frac{\text{NEP}}{\sqrt{\text{BW}}} (\text{W}/\sqrt{\text{Hz}}) \quad (12.6)$$

12.2.5 Detectivity

Detectivity is defined as the reciprocal of NEP value:

$$D = \frac{1}{\text{NEP}} (\text{W}^{-1}) \quad (12.7)$$

The normalized detectivity, D^* , is the most important parameter to characterize the noise performance of photodetectors. In general, the signal increases linearly with the device area, whereas the noise varies with the square root of both the area and the bandwidth. Thus, in order to compare two detectors with different dimensions, the detectivity is normalized for optical area and frequency bandwidth, according to the expression:

$$D^* = D \sqrt{A_{opt} \text{BW}} = \frac{R_i \sqrt{A_{opt} \text{BW}}}{I_n} (\text{W}^{-1} \text{Hz}^{\frac{1}{2}} \text{cm}) \quad (12.8)$$

where A_{opt} is the optical area of the detector. The upper limit of D^* for UV photodetectors is $\sim 10^{17} \text{ W}^{-1} \text{ Hz}^{\frac{1}{2}} \text{ cm}$.

12.3 III-NITRIDE PHOTOCONDUCTORS

$\text{Al}_x\text{Ga}_{1-x}\text{N}$ photoconductors have become the subject of great interest in the last years. Given their simplicity, they were the first candidates for the fabrication of low-cost UV sensors. Their high responsivity, associated with the high internal gain observed in this sort of detectors, makes possible their use without any preamplifier stage. Although the first photoconductivity measurements in GaN were published in 1974 by Pankove and colleagues,¹⁰ only recently have the characteristics of GaN photoconductors been analyzed in detail. Conclusions often depend on the research group, so that it is difficult to distinguish between a general behavior and sample-dependent characteristics. However, there is general agreement on some features, such as the presence of high responsivity ($> 100 \text{ A/W}$),^{11–15} which depends on the light modulating frequency,^{13,16–19} and decreases for increasing illumination power.^{12,14,15,17,20} Also, most of the works report on persistent photoconductivity (PPC) effects,^{12,14–17,19,21–32} that is, the photoinduced increase of the device conductance remains for a long time after removing the light source.

In this section, the general principles of photoconductor operation are first described, followed by discussion of the results obtained in III-nitride based photoconductors, together with different models proposed to explain their performance.

12.3.1 General Principles

A photoconductor is the simplest semiconductor detector. It consists in a bar of material with two Ohmic contacts (see Figure 12.2), and it behaves as a radiation sensitive resistor. The device is biased with a voltage source, and the variation of its conductivity is obtained from the voltage drop in a small load resistor, ΔV , as shown in Figure 12.2.

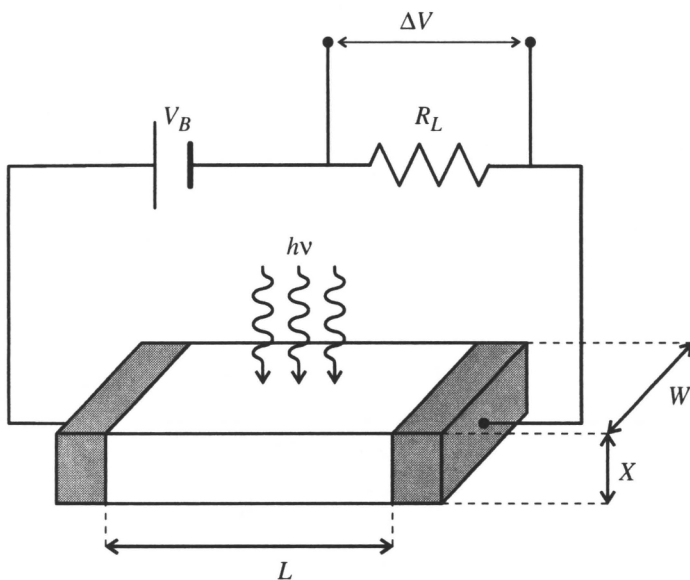


Figure 12.2 Schematic structure of a photoconductor.

12.3.1.1 Responsivity

If the load resistance is small compared with the photoconductor resistance, the voltage drop in the device can be considered approximately equal to the bias voltage, V_B , so that the responsivity is given by:

$$R_i = \frac{I_{ph}}{P_{opt}} = \frac{V_B}{P_{opt}} \Delta G \quad (12.9)$$

where ΔG is the photoinduced variation of the device conductance.

The conductance, G , of a semiconductor bar in the dark can be expressed as:

$$G = q(\mu_e n + \mu_h p) \frac{S}{L} \quad (12.10)$$

where q is the electron charge, μ_e and μ_h are the electron and hole mobilities, respectively, n and p are the electron and hole densities, respectively, $S = w \cdot d$ is the bar section, and L is the distance between contacts.

In an ideal semiconductor, photogenerated carriers may have a very high energy just after ionization. However, they rapidly (in picoseconds) acquire the average thermal energy of carriers in equilibrium, by interaction with phonons and defects. Thus, the energy distribution of carriers under

illumination is the same that in the dark, and the electron and hole mobilities remain constant. The conductance increase under illumination, in steady-state conditions, is given by

$$\Delta G = q(\mu_e \Delta n + \mu_h \Delta p) \frac{S}{L} \quad (12.11)$$

In the case of intrinsic (band-to-band) absorption:

$$\Delta n = \Delta p = \eta \frac{\tau P_{opt}}{d A_{opt} h\nu} \quad (12.12)$$

where η is the quantum efficiency, τ is the carrier lifetime, d is the layer thickness, and $A_{opt} = w \cdot L$ is the optical (exposed) area of the device.

Assuming $\mu_e \gg \mu_h$, the responsivity is obtained from Eqs. (12.9) to (12.12):

$$R_i = \frac{q\eta\tau V_B \mu_e}{h\nu L^2} \quad (12.13)$$

It is important to note the restrictions of these equations. In polycrystalline semiconductors, for instance, light not only increases the free carrier density but also induces changes in the energy band diagram, due to the redistribution of trapped charge in grain boundaries. As a result, to properly explain the behavior of photoconductors in those materials, it is necessary to consider a light-induced variation of either the carrier mobility or the conductive section.

12.3.1.2 Time response

For an ideal semiconductor, without carrier traps and surface effects, the time response is given by the charge conservation equation, expressed as:

$$\frac{d\Delta n}{dt} = R_G - \frac{\Delta n}{\tau} \quad (12.14)$$

where R_G is the generation rate, and τ is the carrier lifetime. Therefore, when removing the light source, the excess of carriers decreases exponentially:

$$\Delta n(t) = \Delta n_0 \exp\left(\frac{-t}{\tau}\right) \quad (12.15)$$

and the photocurrent decay is described by:

$$I_{ph}(t) = \frac{q V_B \mu_e S}{L} \Delta n(t) = I_{ph0} \exp\left(\frac{-t}{\tau}\right) \quad (12.16)$$

In this case, with an exponential transient response, the variation of the responsivity with frequency is given by:

$$R_i(f) = \frac{R_i(0)}{\sqrt{1 + (2\pi f \tau)^2}} \quad (12.17)$$

where $R_i(0)$ is the static responsivity, $R_i(f)$ is the responsivity at frequency, f , and τ is the time constant of the photocurrent decay, which coincides with the lifetime of the excess of carriers.

12.3.1.3 Noise

The main noise sources that may affect the performance of photoconductive detectors are thermal noise, generation-recombination, and $1/f$ noise.⁷ In general, $1/f$ noise is higher at low frequencies, whereas at high frequencies the other noise sources become dominant.

Thermal noise is a white noise associated with the device resistance, R . It is due to the thermal movement of carriers in the crystal, not to the fluctuations in the total number of carriers. The thermal noise power spectral density is given by:

$$S_{nT} = \frac{4kT}{R} \quad (12.18)$$

where k is Boltzmann's constant, and T is the temperature.

Generation-recombination noise is due to the fluctuations in the free carrier density, introduced by random generation and recombination of carriers, either band-to-band or trap-assisted. The generation-recombination noise power spectral density is frequency-dependent. There are several theoretical expressions of this noise power, depending on the semiconductor's internal properties.^{33,34} When the noise arises from deep levels with a well-defined time constant, the noise power spectral density presents a Lorentzian shape, which can be described as:

$$S_{nGR}(f) = \frac{S_0}{1 + 2\pi \tau f} \quad (12.19)$$

where S_0 is a constant, f is the frequency, and τ is the time constant characteristic of the deep level, which is related to its emission, τ_e , and capture, τ_c , time constants, according to the expression:

$$\frac{1}{\tau} = \frac{1}{\tau_e} + \frac{1}{\tau_c} \quad (12.20)$$

12.3.2 Responsivity

Due to the presence of persistent photoconductivity effects, the results of any responsivity measurement depend drastically on the light-modulating frequency and on the time that the sample has been kept in the dark. To avoid the influence of the background current, that is, the dark current that the sample presents at a certain time, Qiu and Pankove²¹ propose that the characterization of these devices should be performed by means of synchronous detection techniques, using a chopper and a lock-in amplifier. However, Monroy and coworkers¹⁹ observe that the dependence on the chopping frequency affects not only the absolute value of the responsivity but also its variation with the incident optical power and with the excitation wavelength. Therefore, in order to obtain reliable and reproducible information about the mechanisms involved in the behavior of these devices, it is necessary to perform their characterization under continuous illumination.

12.3.2.1 Variation with incident power and temperature

The variation of the gain of a GaN photoconductor with the incident power and temperature, measured under continuous excitation, is shown in Figure 12.3. The gain scales proportionally to $P_{opt}^{-\gamma}$, with $0.6 < \gamma < 0.95$, depending on the sample and on temperature.^{14,15,22} This result is independent of the excitation wavelength, either above or below the cutoff edge, as shown in the inset of Figure 12.3. The same behavior is obtained in $\text{Al}_x\text{Ga}_{1-x}\text{N}$ photoconductors.¹⁵

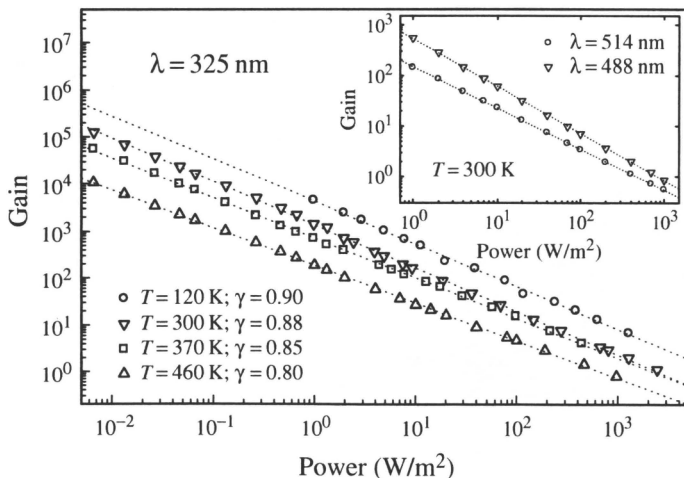


Figure 12.3 Responsivity dependence on the incident optical power, measured in a GaN photoconductor at different temperatures (after Ref. 22).

Stevens and co-authors²³ and Binet and colleagues¹² also report a decrease of the responsivity with optical power. For high irradiance ($>100 \text{ W/m}^2$), the responsivity scales as $R_i \propto P_{opt}^{-0.5}$, and it becomes constant for lower power. Miragliotta and Wickenden²⁰ observe a sublinear behavior: $R_i \propto P_{opt}^{-\gamma}$, with γ varying between 0.9 and 0.5, depending on the sample.

Contradictory data have been published regarding the thermal evolution of the responsivity, because the measuring set-up determines the results. Figure 12.3 shows a clear decrease of the responsivity with temperature, in agreement with the results by Polyakov and co-authors²⁴ and Hirsch and colleagues,²⁵ measuring under continuous illumination. However, Binet and coworkers¹² and Qiu and coworkers²⁶ observe an increase of the responsivity with temperature. This increase would be justified if the measurements had been performed with a lock-in amplifier, due to the thermal acceleration of the persistent phenomena.

12.3.2.2 Spectral response

The spectral response of $\text{Al}_x\text{Ga}_{1-x}\text{N}$ photoconductors, measured under continuous excitation, is shown in Figure 12.4 for samples with different Al composition.¹⁵ The data have been corrected taking into account the lamp spectrum and the optical power dependence shown in Figure 12.3.

The spectra exhibit a maximum, whose position varies between 362 nm and 368 nm for GaN, depending on the sample, and shifts to shorter wavelengths with Al content. The excitonic nature of this peak was demonstrated by Binet and colleagues.³⁵ At room temperature, the free excitons are nearly completely ionized. Thus, at low electric fields, electrons and holes are separated producing a photocurrent. However, as the field increases, the excitonic absorption is quenched by the Franz-Keldysh effect. This evolution is described in Figure 12.5. On the other hand, at low temperature, the exciton is not thermally ionized and it dominates the absorption spectrum. However, the exciton is so stable that it cannot be ionized by a small electric field, thus, it is barely visible in the photoconductor spectral response. To enhance the excitonic peak in the photoresponse at low temperature, it is necessary to increase the applied bias.³⁵

The spectral response for photon energies below the bandgap displays a poor UV/visible contrast, hardly reaching a factor of 10.^{14,15,22} The responsivity drops sharply from 365 nm to 375 nm, and it decreases exponentially for longer wavelengths.

12.3.2.3 Responsivity models

The mechanism involved in the photoconductive responsivity cannot be determined by the optical absorption in the semiconductor alone, because the response to excitation below the bandgap is much higher than expected.

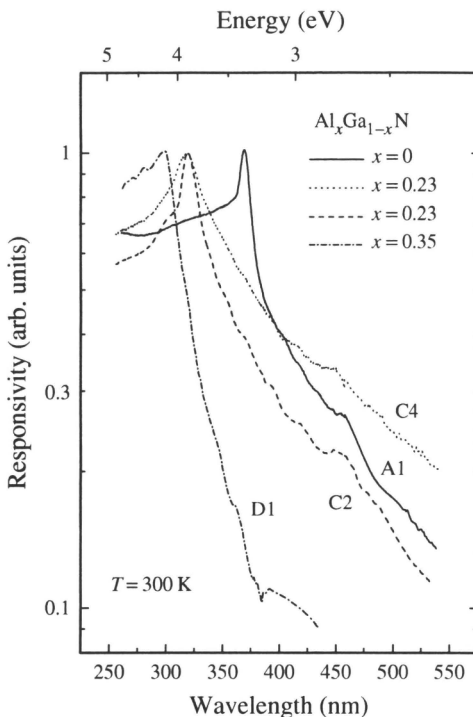


Figure 12.4 Normalized spectral responsivity of different Al contents and Si doping (A1: n.i.d., C2: $N_D = 6.1 \times 10^{17} \text{ cm}^{-3}$, C4: $1.7 \times 10^{18} \text{ cm}^{-3}$, D1: $2.0 \times 10^{18} \text{ cm}^{-3}$) (after Ref. 15).

This fact, together with the sublinear dependence of photocurrent on optical power and the presence of persistent effects, not detected in the same material under the photovoltaic configuration,¹⁹ supports the photoconductive mechanism described by Garrido and co-authors.³⁶ This model assumes that the current responsivity, R_i , consists of two terms: one due to the photogenerated free carriers, Δn , and the other due to the light induced modulation of the effective conduction section, ΔS :

$$R_i = \frac{I_{ph}}{P_{opt}} = \frac{q V_B \mu_e}{L P_{opt}} (\Delta n S + n \Delta S) \quad (12.21)$$

where q is the electron charge, μ_e is the electron mobility, L is the distance between contacts, S is the conductive section, and n is the free carrier concentration.

The conduction section does not correspond to the geometrical section of the devices, due to the presence of depletion regions around lattice

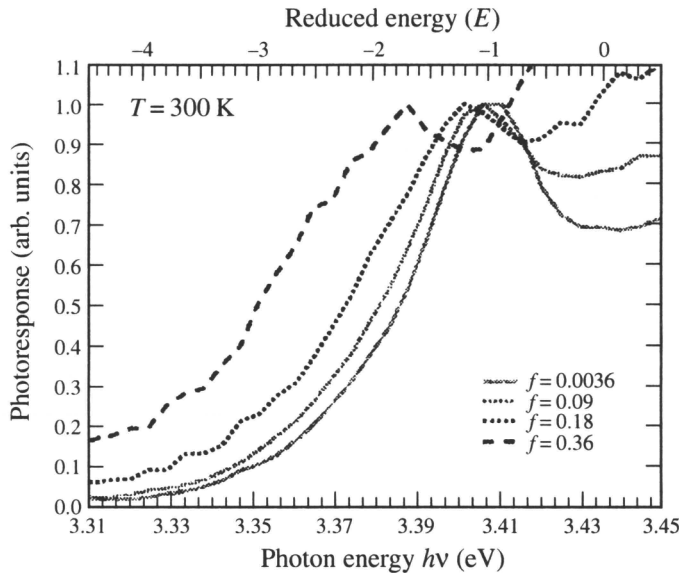


Figure 12.5 Normalized photocurrent spectra of a GaN photoconductor at room temperature, for varying applied fields. The field is defined in reduced units by $f = qFa/R$, where q is the electron charge, F is the electric field, a is the exciton radius and R is the exciton Rydberg (after Ref. 35).

discontinuities (e.g., threading dislocations, grain boundaries, interfaces), like those shown in Figure 12.6. Light induces a shrinking of these depletion regions, modulating the conduction section.

Substituting in Eq. (12.21) the value of Δn ³⁷:

$$\Delta n = \frac{\eta\tau P_{opt}}{SLhc/\lambda} \quad (12.22)$$

where η is the quantum efficiency, g is the photoconductive gain, τ is the excess of free carrier lifetime, and hc/λ is the photon energy, we obtain:

$$R_i = \frac{q\eta\tau V_B\mu_e}{L^2} + \frac{qV_B\mu_e}{LP_{opt}}n\Delta S \quad (12.23)$$

The first term in this equation, due to the light-induced increase of free carriers, corresponds to the classical theory of photoconductors (see Eq. (12.13)), and is independent of the optical power. The spectral dependence of this first term is given by $\lambda \times \eta(\lambda)$. Because the quantum efficiency is a direct function of the absorption coefficient, a good visible rejection would be expectable if this term were dominant.

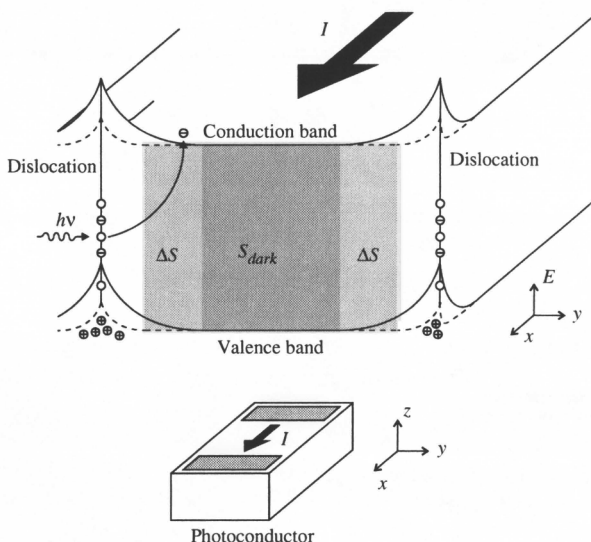


Figure 12.6 Diagram of the energy bands in a section of the photoconductor perpendicular to the current flux. Dashed lines indicate the shrink of the band-bending around dislocations under illumination (after Ref. 19).

However, the dependence of photoconductive responsivity on optical power deduced from Figure 12.3 suggests that the dominant mechanism in these detectors correspond to the second term of Eq. (12.23), that is, to the modulation of the effective conduction section. This mechanism also explains the high response below the bandgap: The levels responsible for visible absorption can be due either to defects distributed throughout the semiconductor (e.g., dopants or vacancies), or to defects localized at lattice discontinuities (e.g., dislocations, grain boundaries, interfaces). If charged, these defects originate a depletion region around them, reducing the effective conduction section of the device (see Figure 12.6). Total light absorption by those defects may be negligible, so that they hardly affect transmission measurements, but their effect on the conductive section of the device is significant.

Neglecting the effect of the first term of Eq. (12.23), the responsivity can be approximated by³⁶:

$$R_i = \frac{n V_B \mu_e A_{opt}}{L^2 P_{opt}} \sqrt{\frac{2q\epsilon_S\epsilon_0}{N_D}} \left(\sqrt{\Psi_0} - \sqrt{\Psi_{il}} \right) \quad (12.24)$$

where A_{opt} is the optical area of the device, ϵ_S and ϵ_0 are the semiconductor dielectric contact and the vacuum permittivity, and Ψ_0 and Ψ_{il} are

the barrier height around the defect in the dark and under illumination. The photogenerated voltage, $V_{ph} = \Psi_o - \Psi_{il}$, can be obtained as³⁶:

$$V_{ph} = \frac{kT}{q} \ln \left[1 + \frac{q\lambda\eta P_{opt}}{hcA^*T^2} \exp \left(\frac{q\Psi_0}{kT} \right) \right] \quad (12.25)$$

where A^* is Richardson's constant. A numerical simulation of Eqs. (12.24) and (12.25) provides the dependence of the photoconductor gain with optical power and temperature shown in Figure 12.7, in agreement with the experimental results.

Salzman and coworkers³⁸ propose a similar model to explain the transport properties of GaN layers. Both the high gain in photoconductors and the persistent photoconductivity are successfully explained by the presence of potential barriers around grain boundaries. However, in their calculations, these researchers prefer to consider the area as a constant and to analyze the effect of the light-induced modulation of the SCRs on the carrier mobility.

A decrease of the responsivity with optical power was also observed in GaAs photoconductors.^{39,40} Moreover, Vilcot and colleagues³⁹ detected a gain decrease with temperature, in agreement with Monroy and coworkers.^{15,22} These phenomena were attributed to a spatial separation of electrons and holes due to the band-bending in the semiconductor surface.³⁹

The importance of band-bendings in grain boundaries, and their effect in photoconductivity, were analyzed by Orton and co-authors⁴¹ in

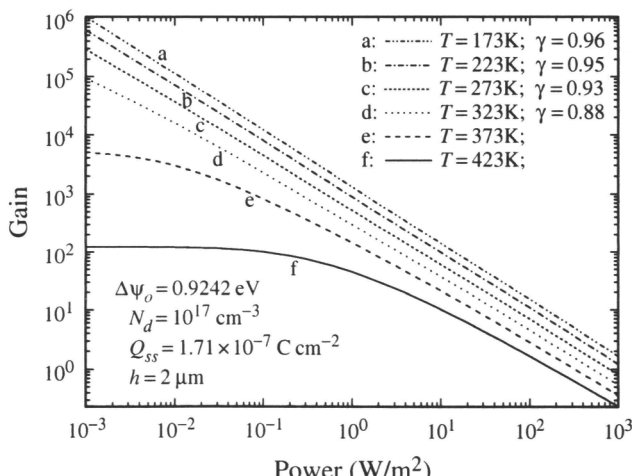


Figure 12.7 Computer simulations of the photoconductor gain vs. irradiance and temperature (after Ref. 36).

polycrystalline CdS. The results were explained by means of Petritz's theory of the conductivity in polycrystalline materials,⁴² in which the existence of a space charge region (SCR) in the grain boundaries limits the carrier mobility in the layer. Illumination provokes a shrink of the SCR, so that the mobility increases. This phenomenon has also been observed in CdSe, Cd(SSe), PbS, and PbTe layers. Petritz's theory is an approach similar to the model described above, by Garrido and others,³⁶ which assumes a constant mobility, whereas the conduction section is modulated by the light intensity. This model makes it possible to include the effect of the SCR due to the air-semiconductor interface.

Another mechanism which explains the sublinear behavior of these devices is Figiel'ski's model,⁴³ which analyzes the role of dislocations in the photoconductor operation. According to Figiel'ski's equations, the photocurrent should increase with the logarithm of the optical power for highly dislocated semiconductors. The responsivity should also decrease with temperature, in agreement with the results in $\text{Al}_x\text{Ga}_{1-x}\text{N}$ shown in Figure 12.3. Despite the sublinear trend, Figiel'ski's equations do not fit precisely the experimental results. The discrepancy could be related to the fact that Figiel'ski presumes that the photocurrent is proportional to the number of photogenerated carriers, which can come from the bulk or from dislocations. The variation of the SCRs around dislocations and their effect on the conductive section (or in the average mobility) is not considered by this model.

In conclusion, the model based on the modulation of the conductive section can simultaneously explain both the variation of the responsivity with the optical power in $\text{Al}_x\text{Ga}_{1-x}\text{N}$ photoconductors and its temperature dependence.

12.3.3 Time Response

12.3.3.1 Experimental results

One of the most important issues related to the performance of $\text{Al}_x\text{Ga}_{1-x}\text{N}$ photoconductors is slow response time. Most of the research groups working with these detectors have reported the presence of persistent photoconductivity (PPC), that is, the photocurrent persists for a long time (hours) after the light is removed, as seen in Figure 12.8. The photocurrent decays are clearly nonexponential.

PPC has been reported in n.i.d.,^{14,21,22,25,26,30,44–46} *n*-type doped,^{27,30,46} and *p*-type doped^{28,29,44} GaN photoconductors, as well as in $\text{Al}_x\text{Ga}_{1-x}\text{N}$ photoconductors^{15,45} with Al mole fractions up to 0.6. AlGaN/GaN heterostructures^{47–49} also present persistent effects, which are attributed either to deep levels^{47,48} or to potential fluctuations in the channel.⁴⁹

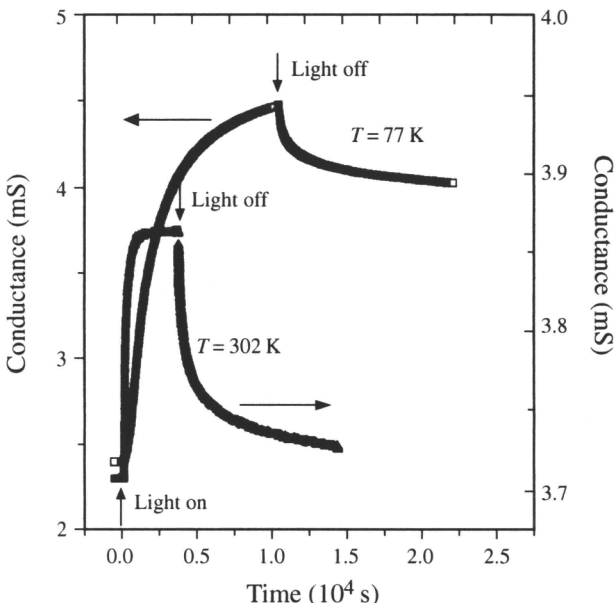


Figure 12.8 Buidup and decay transients of the conductivity at $T = 77\text{ K}$ and $T = 302\text{ K}$ (after Ref. 25).

The photocurrent decays in $\text{Al}_x\text{Ga}_{1-x}\text{N}$ photoconductors are well-fitted by the stretched exponential function:

$$I_{ph}(t) = I_{ph0} \exp[-(t/\tau)^\beta] \quad (12.26)$$

where τ is a time constant, and $\beta < 1$. This equation has been extensively used for photoconductors,^{21,27,30,45,47} and also describes the PPC observed in AlGaAs due to DX centers,⁵⁰ and in ZnCdSe due to potential fluctuations.⁵¹ However, it has not been related to detailed microscopic models, and the values of τ and β are not associated with specific material parameters.

PPC has been reported in a number of materials, and there are several possible sources of persistent effects. It is known that metastable defects induce persistent phenomena, for instance, the DX centers in AlGaAs.^{50,52} Potential fluctuations due to inhomogeneity in ternary compounds have also been probed to generate PPC.⁵¹ Another persistent source is the band-bending at the semiconductor surface.^{39,53} The importance of surface levels on the PPC in GaAs was analyzed in detail by Gouin and co-authors,⁵⁴ who compared the effect on the time response of deep levels in the bulk semiconductor and at the surface. Thus, in order to justify the experimental PPC,

the density of deep levels in the bulk should be so high that there is no doubt that surface levels are playing an important role. Another demonstration of the influence of the surface on the PPC is the fact that a surface chemical etching,⁵⁴ or the deposition of a dielectric layer,⁵⁵ drastically change the time behavior of the photoconductors. In the case of a heterostructure, the band-bending at the interface induces an spacial separation of electrons and holes, which may induce PPC effects, as demonstrated by Collins and colleagues⁵⁶ in AlGaAs/GaAs heterojunctions. Finally, the recombination through dislocations may also result in PPC, as shown by Figielski⁴³ on plastically deformed Si.

In GaN, impurities such as Si or Mg have been proposed as the origin of PPC in doped samples,^{28,29} and oxygen contamination has also been suggested.⁴⁵ PPC has also been attributed to intrinsic material defects, such as Ga vacancies^{21,27} or the defects responsible for yellow photoluminescence emission.^{30,31} In the following sections, the different models proposed to explain the PPC are analyzed.

12.3.3.2 Mid-gap trap

Kung and co-authors¹⁶ and Binet and co-authors¹² explain the nonexponential shape of the photocurrent decays with a model which assumes the presence of a trap level in the bandgap, which is ionized by the incident radiation. When the light is removed, ionized traps behave as recombination centers, whose efficiency decreases with time, as they recapture electrons. Assuming a trap level with a state density, N_T , and an occupation, n_T , the carrier dynamics may be expressed by the following Eq. (12.12):

$$\left. \begin{aligned} \frac{dn}{dt} &= G_{opt} + G_{th} - \gamma np - \beta_n(N_T - n_T) \\ \frac{dn_T}{dt} &= \beta_p n_T p - \beta_n(N_T - n_T) \\ \frac{dp}{dt} &= G_{opt} + G_{th} - \gamma np - \beta_p n_T p \end{aligned} \right\} \quad (12.27)$$

where G_{opt} and G_{th} are the optical and thermal generation rates, and β_n and β_p are:

$$\beta_n = \sqrt{\frac{3KT}{m_e^*}} \sigma_e \quad \text{and} \quad \beta_p = \sqrt{\frac{3KT}{m_h^*}} \sigma_h \quad (12.28)$$

where m_e^* and m_h^* are the effective masses, and σ_e and σ_h the capture sections for electrons and holes, respectively.

This model provides a good fit for the first milliseconds of the photocurrent decays and their dependence on the optical power,¹² but it fails to explain

the long nonexponential tails observed by most of the groups working with $\text{Al}_x\text{Ga}_{1-x}\text{N}$ photoconductors.

12.3.3.3 Metastable (DX-like) defects

There are some theoretical and experimental studies seeking metastable defects that could be responsible for PPC in GaN and $\text{Al}_x\text{Ga}_{1-x}\text{N}$. Some calculations indicate that Si and Ge should behave as DX centers for high Al contents,^{57–59} whereas Van de Walle⁶⁰ shows that the formation of a Si localized state is energetically unfavorable for the whole composition range of $\text{Al}_x\text{Ga}_{1-x}\text{N}$. According to the experimental results of Polyakov and colleagues,⁴⁵ the activation energy of Si evolves from 18 meV for GaN, to 50 meV for $x = 0.4$, and it is not higher than 90 meV for $x = 0.6$. These values indicate that the transition from shallow donor to deep donor, characteristic of a DX center, is not present for Al mole fractions lower than 0.6. Moreover, Raman dispersion measurements as a function of hydrostatic pressure indicate that Si only introduces a deep level in GaN for a pressure equivalent to an Al content of at least 40 percent.⁶¹ On the other hand, by pressure-dependent transport measurements, Skiebiszewski and co-authors⁶² observed a metastable behavior in the level introduced by Si in $\text{Al}_x\text{Ga}_{1-x}\text{N}$ for $x > 0.5$, which provokes persistent effects. All these results indicate that Si is not responsible for the PPC observed in $\text{Al}_x\text{Ga}_{1-x}\text{N}$ for low Al concentrations ($x < 0.4$), although it behaves as a DX center for high Al mole fractions.

It has also been suggested that Si might introduce potential fluctuations in GaN.⁶³ However, the PPC due to potential fluctuations can be identified by its quenching when illuminating with energy below the bandgap.⁶⁴ A reduction of the photocurrent when illuminating the devices with an He-Ne laser ($\lambda = 632.8$ nm) has been reported,^{65,66} but this is not a typical behavior.

Theoretical evidences also exist that hydrogen and hydrogenated compounds behave as DX centers in GaN.⁶⁷ Based on these calculations, Johnson and coworkers²⁹ explain the PPC in Mg-doped samples grown by MOVPE as due to two impurity levels, one metastable and the other one stable, which might be related to H and Mg-H complexes, respectively. However, H concentrations in MBE grown material are too low to justify the PPC observed in Mg-doped samples grown by this technique. Thus, Li and colleagues²⁸ suggest that Mg itself could be responsible for the persistent effects. This statement contradicts the theoretical studies by Park and Chadi,⁵⁸ who concluded that the shallow acceptor configuration of Mg is more stable than the deep level configuration. Instead, the latter authors propose that the origin of PPC in these samples could be due to the bistability of the N vacancy associated with Mg.

On the other hand, it is known that O, which behaves like a shallow donor in GaN, introduces a deep level under pressures equivalent to an aluminum content of 30 percent to 40 percent,⁶⁰ in agreement with theoretical studies predicting a DX behavior for O in $\text{Al}_x\text{Ga}_{1-x}\text{N}$.^{59,68} According to Van de Walle and coworkers,⁶⁸ the O-related persistent photoconductivity should appear only for temperatures below 150 K, with a photoionization threshold of 1.3 eV. These characteristics have been observed by McCluskey and colleagues⁶⁹ in $\text{Al}_x\text{Ga}_{1-x}\text{N}$ samples with an O content of 10^{19} cm^{-3} , measured by SIMS. Polyakov and coworkers⁴⁵ reported the same characteristics in n.i.d. and Si-doped $\text{Al}_x\text{Ga}_{1-x}\text{N}$ layers, although they do not mention the O concentration in their material. However, as discussed by Van de Wall and colleagues,⁶⁸ this behavior does not coincide with the PPC reported by other authors,^{19,25,27} thus, only in certain cases could O be responsible for the PPC in $\text{Al}_x\text{Ga}_{1-x}\text{N}$.

The most common explanation of the persistent effects in GaN relates this phenomenon to the defects responsible for the photoluminescence yellow band.^{30,31} According to Reddy and co-authors,³¹ this explanation is supported by three facts: (1) there is no PPC in cubic GaN without yellow band; (2) the response to photons with an energy of 1.77 eV is faster than in the case of 1.96 eV; and (3) no response is registered for photons with energy lower than 1.6 eV. The latter statement, however, disagrees with other observations.⁴⁶ It has also been reported that there is no correlation between the yellow luminescence intensity and the photoconductor speed.⁴⁶ Moreover, persistent phenomena have been detected in $\text{Al}_x\text{Ga}_{1-x}\text{N}$ layers without yellow band.¹⁵

12.3.3.4 Modulation of the conduction section

The presence of PPC can be justified by the same mechanism responsible for the high gain in these devices.^{15,36} The photoionization of electrons trapped at defects provokes a variation of the charge in those defects and, therefore a shrinking of the SCRs around them. Because of the band-bending, holes are trapped at defects and, when the light is off, electrons must cross a potential barrier prior to recombination. Because the barrier height increases with the square of the charge at the defect, the current decay is nonexponential.

This model can be applied if the dominant defects are located either in dislocations or grain boundaries, or at the $\text{Al}_x\text{Ga}_{1-x}\text{N}$ -air or $\text{Al}_x\text{Ga}_{1-x}\text{N}$ -substrate interfaces. However, it is difficult to discriminate between these two regions, whose relative importance might depend on the material quality. Salzman and coworkers³⁸ locate the potential barriers in the gain boundaries. However, the contribution to responsivity and PPC by the $\text{Al}_x\text{Ga}_{1-x}\text{N}$ -substrate surface has been demonstrated by Seifert and co-authors,³² who observed an increase of photocurrent and PPC when illuminating through the substrate (sapphire). However, with front illumination above the bandgap,

the light does not reach the substrate, so that in this case PPC should be related to the $\text{Al}_x\text{Ga}_{1-x}\text{N}$ -air interface or to dislocations and grain boundaries. Regarding dislocations, Hansen and colleagues,⁷⁰ using a capacitance scanning microscope, detected charged regions around threading dislocations in GaN, which could originate the persistent behavior. There have not been many studies of the GaN-air interface. Bermudez and colleagues⁷¹ measured by means of x-ray photoelectron spectroscopy (XPS) a surface band-bending of 1.5 eV for atomically clean material, decreasing to 1.0 eV after maintaining the sample in an O-rich atmosphere.⁷²

The increase of the charge trapped at a defect, ΔQ_{SS} , is related to the variation of the SCR width, Δx_{SCR} , by:

$$\Delta Q_{SS} = q N_D \Delta x_{SCR} = \sqrt{2q N_D \varepsilon_S \varepsilon_0} \left(\sqrt{\Psi_0} - \sqrt{\Psi_{il}} \right) \quad (12.29)$$

so that Eq. (12.24) can be written as:

$$R_i = \frac{A_{opt} V_B \mu_e}{P_{opt} L^2} \Delta Q_{SS} \quad (12.30)$$

and the photocurrent varies with the charge density at the defect, and with time, according to the expression:

$$I_{ph}(t) = \frac{A_{opt} V_B \mu_e}{L^2} \Delta Q_{SS}(t) \quad (12.31)$$

In the dark, the variation of the charge at the defect is due to the current crossing the potential barrier around the defect, either by thermionic emission, J_{th} , or by thermionic field emission, J_{tunnel} (tunnel transport component)¹⁵:

$$\frac{dQ_{SS}(t)}{dt} = J_{th} + J_{tunnel} \quad (12.32)$$

being the currents given by:

$$J_{th} = A^* T^2 \exp\left(-\frac{q\Phi_0}{kT}\right) \left[\exp\left(\frac{qV_{ph}}{kT}\right) - 1 \right] \quad (12.33)$$

and

$$J_{tunnel} = A^* T^2 \frac{\sqrt{\pi E_{00}(\Psi_0 - V_{ph})}}{(kT/q) \cosh(qE_{00}/kT)} \exp\left(-\frac{q(\Psi_0 - V_{ph})}{E_0}\right) \times \left[1 - \exp\left(\frac{qV_{ph}}{kT}\right) \right] \quad (12.34)$$

where

$$E_0 = E_{00} \coth \left(\frac{qE_{00}}{kT} \right) \quad (12.35)$$

$$E_{00} = \frac{h}{4\pi} \left(\frac{N_D}{m^* \epsilon} \right) \quad (12.36)$$

and the photogenerated voltage, V_{ph} , can be expressed as:

$$V_{ph}(t) = \Psi_0 - \frac{Q_{SS}^2(t)}{2q\epsilon_S \epsilon_0 N_d} \quad (12.37)$$

This model has been implemented by computer for samples with different n -type doping concentrations, and the simulation achieves a good agreement with experimental data, as shown in Figure 12.9. The importance of tunnel recombination, which increases with time and dominates the response even in the undoped sample, is shown in the inset of Figure 12.9. Tunnel rates increases with Si concentration, which explains the faster device relaxation in Si-doped detectors.

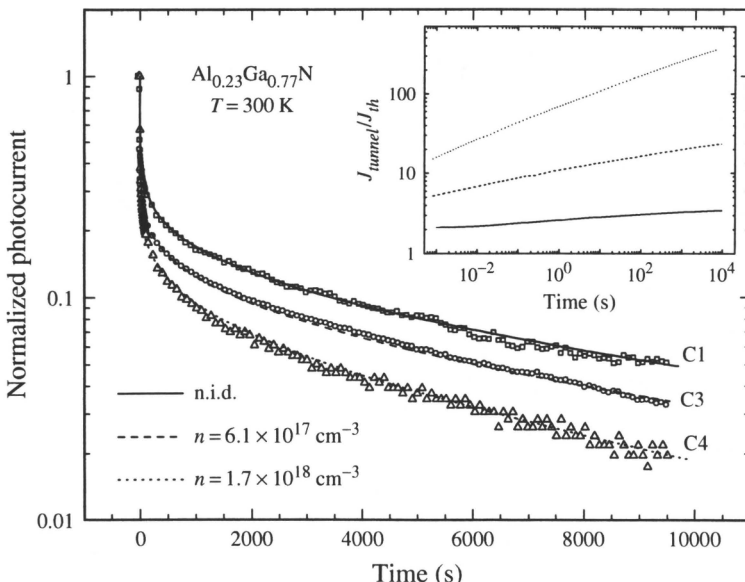


Figure 12.9 Normalized photocurrent decays of $\text{Al}_{0.23}\text{Ga}_{0.77}\text{N}$ photoconductors, after an excitation light pulse from an He-Cd laser, and their computer simulation. Insert: evolution of the tunnel:thermionic current ratio with time and Si doping. (after Ref. 15).

In conclusion, there are several defects that could present a metastable behavior in GaN, but they alone cannot justify the persistent photoconductivity observed in undoped, Si-doped, Mg-doped, or Ge-doped GaN and $\text{Al}_x\text{Ga}_{1-x}\text{N}$ samples, grown either by MOVPE or by MBE. Although the contribution of those defects to PPC is not discarded, the model based on the *modulation of the conduction section*^{14,36} explains the behavior of all kinds of samples. Moreover, the mathematical formulation of this model fits precisely the photocurrent decays in these devices.¹⁵

12.3.4 Frequency Response

Photoconductor responsivity has been shown to strongly depend on light modulating frequency,^{13,16–19,21,44} as shown in Figure 12.10. In the analysis of these results, it is frequently assumed that the transient response of the detector is exponential, and the responsivity is proportional to the excess concentration of minority carriers. Thus, the variation of the responsivity with frequency is given by Eq. (12.17). The carrier lifetime is often derived from this equation by fitting this equation to the experimental data. However, taking into account the clear nonexponential behavior observed in the photoconductor time response, the application of Eq. (12.17) is no longer valid for the analysis of these detectors.

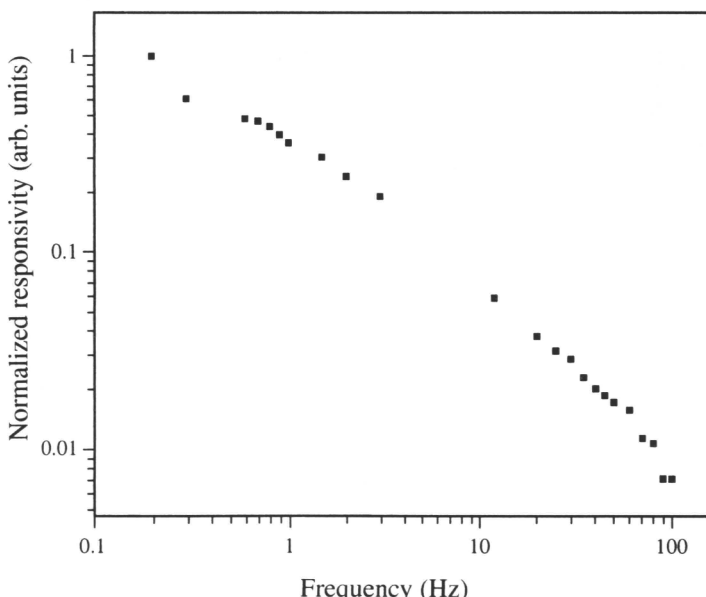


Figure 12.10 Variation of the responsivity with frequency in a GaN photoconductor (after Ref. 17).

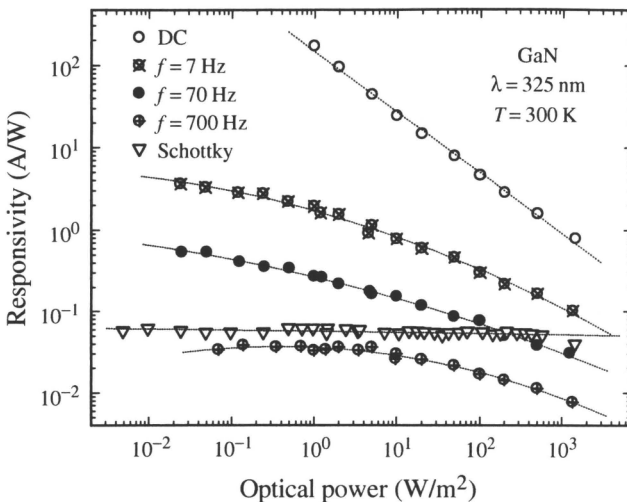


Figure 12.11 Responsivity versus optical power measured in a photoconductor using lock-in detection with different chopping frequencies. Data corresponding to a Schottky photodiode on the same sample are also presented for comparison. (after Ref. 19).

The chopper frequency affects not only the value of the responsivity, but also its dependence on the incident optical power and the spectral response, as demonstrated by Monroy and coworkers.¹⁹ Figure 12.11 shows the dependence of the responsivity on the optical power for different chopping frequencies. The responsivity becomes flatter when the frequency is increased from 7 Hz to 700 Hz.

The effect of frequency on the spectral response is depicted in Figure 12.12. When the mechanism responsible for the PPC is reduced by increasing the chopping frequency, the cut-off becomes sharper and the spectrum below the bandgap tends to the photovoltage response, whose contrast is given by the absorption coefficient of the material.

To interpret these results, it is necessary to analyze the frequency behavior of the responsivity described by Eq. (12.23). The first term of this equation is the responsivity due to the increase of free carriers. It is constant with optical power, and presents a high UV/visible contrast, because its spectral response is given by the semiconductor absorption. The time response of this term is determined by the excess of carrier lifetime, τ , in the nanosecond range.⁷³ Therefore, this contribution to the total responsivity is not affected by the chopping frequency.

The second term of Eq. (12.23) corresponds to the responsivity due to the modulation of the conductive section. It decreases with optical power and it is extremely slow, being responsible for the persistent effects. Thus, this contribution to R_i is strongly frequency-dependent, even for very low frequencies.

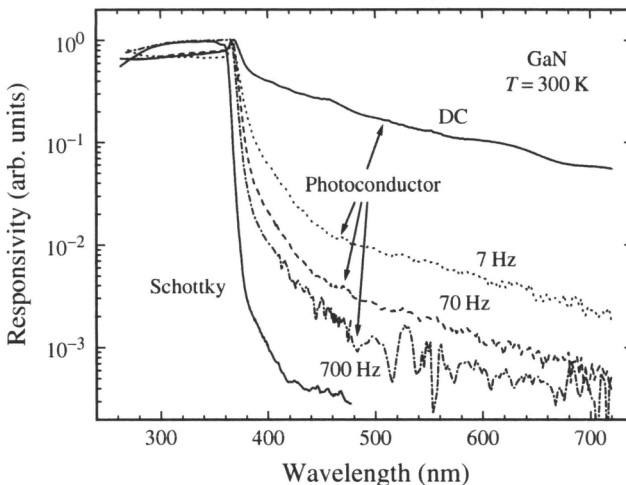


Figure 12.12 Normalized spectral response of a photoconductor measured with the lock-in technique and different chopping frequencies. The spectrum of a Schottky photodiode on the same sample is also shown for comparison. (after Ref. 19).

Regarding the visible contrast, this mechanism is very sensitive to radiation with energy below the semiconductor bandgap, which means a poor UV/visible contrast.

The static behavior of these devices points to the modulation of the conductive section as the dominant mechanism. When increasing the chopping frequency from 7 Hz to 700 Hz, the SCR related to defects do not have enough time to react, so that the responsivity decreases as well as its dependence on optical power (Figure 12.11). For the same reason, the absorption of below-the-bandgap photons decreases, so that the UV/visible contrast increases, as observed in Figure 12.12.

In conclusion, photoconductive detectors are unsuitable for applications requiring speed or a certain spectral contrast, unless lock-in detection is used. In this configuration, however, these devices lose all their advantages, because their responsivity is considerably reduced and the detection system becomes more complex and expensive.

12.3.5 Noise

Misra and colleagues⁷⁴ and D'yakonova and co-authors⁷⁵ have analyzed the low-frequency noise behavior of n.i.d. GaN photoconductive detectors. Measuring in the 10 Hz to 50 KHz range, Misra and colleagues⁷⁴ found that the noise spectrum is dominated by $1/f$ and thermal noise for low-resistivity ($\rho = 10^2 \Omega \text{ cm}$) devices, and by generation-recombination noise

for high-resistivity devices ($\rho = 10^6 \Omega \text{ cm}$), at room temperature. From the evolution with temperature of the generation-recombination noise, a deep level was identified, located about 0.4 eV below the conduction band. Optical excitation revealed the presence of this trap in the low-resistivity material, where it was not observed by thermal excitation.

D'yakonova and co-authors⁷⁵ analyzed $1/f$ noise in the 20 Hz to 20 KHz range. The noise power spectral density behaves as:

$$S_n = \frac{s_0 I_d^2}{f} \quad (12.38)$$

where I_d is the dark current, and s_0 is constant. The variation of the noise level with temperature is weak and nonmonotonic.

The noise properties of different materials are often characterized the dimensionless Hooge parameter, α ⁹:

$$\alpha = s_0 N \quad (12.39)$$

where N is the total number of carriers. D'yakonova and colleagues⁷⁵ obtain $\alpha \simeq 5$ to 7 for GaN. This large value of α indicates poor structural quality, which is justified by the high dislocation densities and internal stresses still present in state-of-the-art GaN.

12.3.6 Photoconductors on Insulating GaN

Highly insulating GaN epitaxial layers can be obtained under certain growth conditions, or by intentionally compensating the residual doping. Photoconductors fabricated on these layers have been reported by several groups.^{76–78} These devices behave linearly with optical power and present a sharper cutoff, with a higher UV/visible ratio. Their performance is similar to metal-semiconductor-metal photodiodes, which are described in Section 12.5.

12.4 SCHOTTKY PHOTODIODES

Although the first Schottky contacts on GaN were reported in the 1970s,⁷⁹ their controlled and reproducible fabrication was not possible until much later. In fact, the first Schottky barrier photodetector was demonstrated in 1993 by Khan and coworkers,⁸⁰ who fabricated a Ti Schottky photodiode on *p*-type GaN. Since then, Schottky technology has evolved considerably. By the beginning of 1998, GaN Schottky photodiodes became the first commercially available III-nitride-based UV photodetectors.

12.4.1 General Principles

Schottky photodiodes consist of an Ohmic contact and a Schottky barrier. This device can be operated as a photovoltaic detector, connected in series with a current amplifier or a load resistance.

12.4.1.1 Responsivity

The electric field in the SCR separates the photogenerated electrons and holes, producing a photocurrent. Carriers generated within a diffusion length of the SCR may diffuse toward it, also contributing to the photocurrent. Finally, another contribution is the electronic emission from the metal over the Schottky barrier height. Thus, the total responsivity is given by:

$$R_i = \frac{(J_{drift} + J_{diff} + J_{emis})A}{P_{opt}} \quad (12.40)$$

where J_{drift} , J_{diff} , and J_{emis} are the current densities due to drift, diffusion, and emission from the metal, respectively, and A is the Schottky contact area.

The drift photocurrent can be expressed as:

$$J_{drift} = -q \int_{SCR} G(x) dx \quad (12.41)$$

where $G(x)$ is the generation rate, given by:

$$G(x) = \Phi_{ph}\alpha e^{-\alpha x} \quad (12.42)$$

where Φ_{ph} is the photon flux reaching the semiconductor, and α is the semiconductor absorption coefficient.

The diffusion photocurrent is given by:

$$J_{diff} = -q D_h \left(\frac{\partial p}{\partial x} \right)_{x=w} \quad (12.43)$$

where D_h is the minority (hole) diffusion constant and $x = w$ is the SCR edge. The hole concentration, $p(x)$, can be obtained from the continuity equation:

$$D_h \frac{\partial^2 p}{\partial x^2} - \frac{p - p_0}{\tau_h} + G(x) = 0 \quad (12.44)$$

where τ_h is the hole lifetime.

The emission photocurrent can be estimated as⁸¹⁻⁸³

$$J_{emis} = -q\Phi_{ph}P_\alpha\eta_{int}\eta_{col} \quad (12.45)$$

where P_α is the metal absorbance, η_{int} is the internal quantum yield, and η_{col} is the collection efficiency, which accounts for electron scattering from the surfaces, phonons, and cold electrons. The internal quantum yield is defined as the probability that an excited electron will “escape” into the semiconductor. This yield is approximated by Fowler’s equation⁸⁴:

$$\eta_{int} = \frac{(hv - q\Phi_0)^2}{4\phi_m hv} \quad (12.46)$$

where $q\Phi_0$ is the Schottky barrier height, and ϕ_m is the metal work function.

12.4.1.2 Time response

The time response of Schottky photodiodes is most commonly limited by the RC product of the system, where R is the sum of the load resistance, R_L , and the diode series resistance, R_S , and C is the diode capacitance, given by:

$$C = A\sqrt{\frac{qN_D\varepsilon_s\varepsilon_0}{2(\Psi_0 + V_B)}} \quad (12.47)$$

where A is the Schottky contact area, Ψ_0 is the barrier height seen from the semiconductor, and V_B is the bias voltage. Thus, the device time constant increases with the Schottky contact area, being $C \propto A$, and the application of reverse bias implies a reduction of the diode capacitance.

12.4.1.3 Noise

There are basically three noise components in a Schottky diode: $1/f$ noise, shot noise, and thermal noise, due to the device series resistance.

The thermal noise power spectral density is given by:

$$S_{nT} = \frac{4kT}{R_0} \quad (12.48)$$

where R_0 is the diode shunt resistance.

In order to evaluate the shot noise power spectral density, the diode current to voltage characteristic is approximated by:

$$I(V) = I_{sat} \left[\exp\left(\frac{qV}{\beta kT}\right) - 1 \right] \quad (12.49)$$

where I_{sat} is the saturation current, and β is the ideality factor. This current consists of two components: one due to the carrier flux from the semiconductor toward the metal, $I_{sat} \exp(qV/\beta kT) = I(V) + I_{sat}$, and the other due to the carrier flux from the metal to the semiconductor, I_{sat} . Both currents fluctuate independently and contribute to the shot noise. Moreover, when the diode is under illumination, it is necessary to take into account the shot noise due to fluctuations in the photocurrent, I_{ph} , so that the total shot noise power spectral density, S_{sn} , is given by:

$$S_{sn} = 2q(I + 2I_{sat} + I_{ph}) \quad (12.50)$$

In general, at high frequencies shot noise is dominant, whereas at low frequencies $1/f$ noise can be higher. Thermal noise is usually negligible, compared with the other noise sources.

12.4.2 Device Structures and Responsivity

Different device structures have been tested for $\text{Al}_x\text{Ga}_{1-x}\text{N}$ based Schottky photodiodes, including backside illumination, and frontside illuminated vertical and planar geometries. A schematic diagram of these structures is shown in Figure 12.13.

12.4.2.1 Backside illumination

The first GaN-based Schottky barrier photodiodes⁸⁰ consisted of a Ti/Au Schottky contact (1500-Å thick) surrounded by a ring-shaped Cr/Au Ohmic contact on 2-μm-thick Mg-doped GaN layers. The Schottky barrier diameter ranged from 200 μm to 1 mm. The devices showed a zero-bias responsivity of 130 mA/W, and the UV/visible contrast of these devices was about 100,

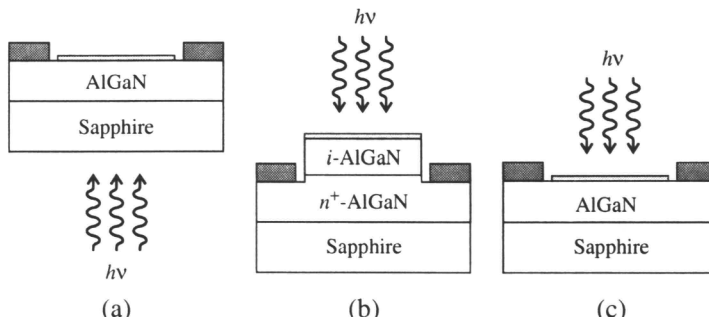


Figure 12.13 Schematic diagram of different geometries for AlGaN Schottky photodiodes: (a) backside illumination; (b) frontside illumination, vertical structure, and (c) frontside illumination, planar structure.

illuminating through the transparent substrate (sapphire). The time response was *RC*-limited, with an estimated time constant (time for the signal to fall from maximum to $1/e$) of around 1 μs for diodes with a diameter of 1 mm.

The inconvenience of backside illumination was analyzed by Binet and co-authors⁸⁵ on a Pt/Au Schottky barrier on n.i.d. GaN. The sample GaN epilayer was 2.6 μm thick and the residual donor density was estimated to be $3 \times 10^{16} \text{ cm}^{-3}$. The maximum responsivity was very low, about 3 mA/W, and decreased markedly for excitation above the bandgap, which showed a poor carrier collection efficiency. In this configuration, holes photogenerated near the substrate must diffuse until the Schottky contact were they are collected. From a simple model, a hole diffusion length of 0.1 μm is calculated for these structures,⁸⁵ which limits the above-the-bandgap responsivity. This diffusion length agrees with the value estimated by Zhang and colleagues⁸⁶ from the response of a backside illuminated p-n junction.

12.4.2.2 *Frontside illumination, vertical structure*

The problem of diffusion length is solved by front illumination through a semitransparent Schottky contact. Chen and coworkers⁸⁷ reported a semitransparent 50 Å Pd Schottky barrier on an n^-/n^+ (0.4 $\mu\text{m}/1 \mu\text{m}$) GaN structure (see Figure 12.13b), with a responsivity of about 180 mA/W and an *RC*-limited time response of 118 ns on a 50- Ω resistance. The spectral response was approximately constant for photon energies above the bandgap and showed an abrupt cutoff.

$\text{Al}_{0.26}\text{Ga}_{0.74}\text{N}$ Schottky photodiodes with the same vertical structure and different active areas, ranging from $50 \times 50 \mu\text{m}^2$ to $500 \times 500 \mu\text{m}^2$, have also been reported.⁸⁸ These devices showed a responsivity of 70 mA/W and an *RC*-limited time response with a minimum decay time of 1.6 μs .

12.4.2.3 *Frontside illumination, planar structure*

Planar Schottky devices are based on moderately *n*-type doped $\text{Al}_x\text{Ga}_{1-x}\text{N}$ epitaxial layers, and they do not require semiconductor etching. semitransparent Au and Ni devices have been reported on $\text{Al}_x\text{Ga}_{1-x}\text{N}$ layers with an Al mole fraction up to 35 percent.^{89–92} Device diameters ranged from 200 μm to 1 mm. In these devices, the photocurrent increases linearly with optical power, both for excitation above and below the bandgap, over more than five decades, as shown in Figure 12.14. Above-the-bandgap responsivities of 54 mA/W, 45 mA/W, 30 mA/W, and 10 mA/W have been measured for $x = 0, 0.15, 0.22$, and 0.35, respectively. No temperature dependence of the photodiode responsivity has been observed in the range from -150°C to 150°C .⁸⁹

Figure 12.15 shows the typical spectral response of Au photodiodes. A visible rejection of about 10^3 is obtained for all the devices, which is similar to results obtained with Pd (see Figure 12.16). The UV visible contrast

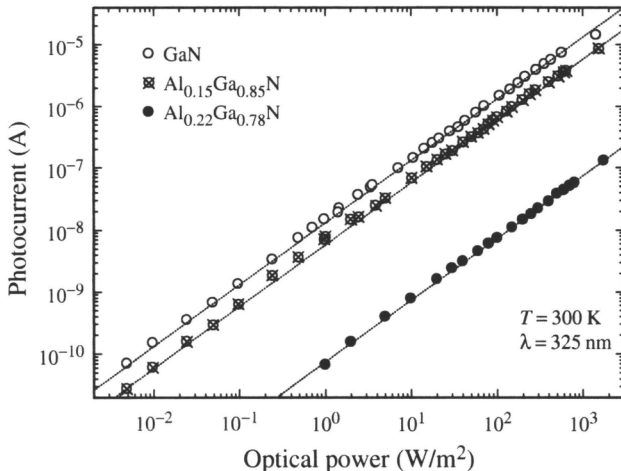


Figure 12.14 Photocurrent measured on $\text{Al}_x\text{Ga}_{1-x}\text{N}/\text{Au}$ Schottky photodiodes ($x = 0, 0.15$, and 0.22), with a He-Cd laser ($\lambda = 325 \text{ nm}$) (after Ref. 90).

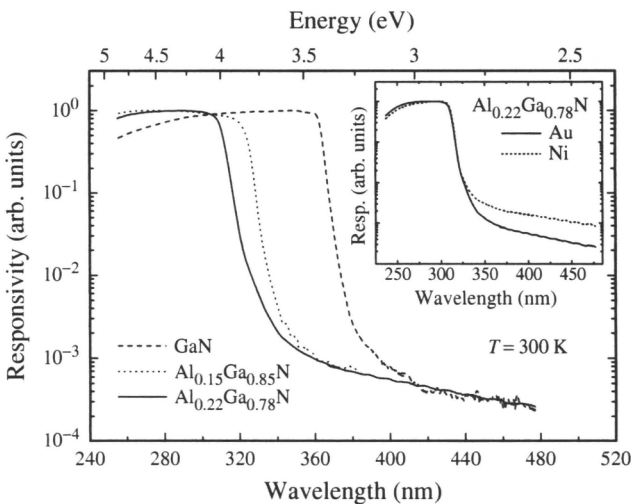


Figure 12.15 Normalized spectral response of $\text{Al}_x\text{Ga}_{1-x}\text{N}/\text{Au}$ Schottky photodiodes ($x = 0, 0.15$, and 0.22). In the inset, comparison of the spectral response of Au and Ni detectors fabricated on $\text{Al}_{0.22}\text{Ga}_{0.78}\text{N}$ layers (after Ref. 90).

was found to be lower in Ni devices, as observed in the inset of Figure 12.15, probably due to electron photoionization from the metal, enhanced by the lower barrier height measured in these devices ($q\Phi_0 = 0.7 \text{ eV}$ in GaN/Ni versus 0.9 in GaN/Au). The responsivity is quite flat above the

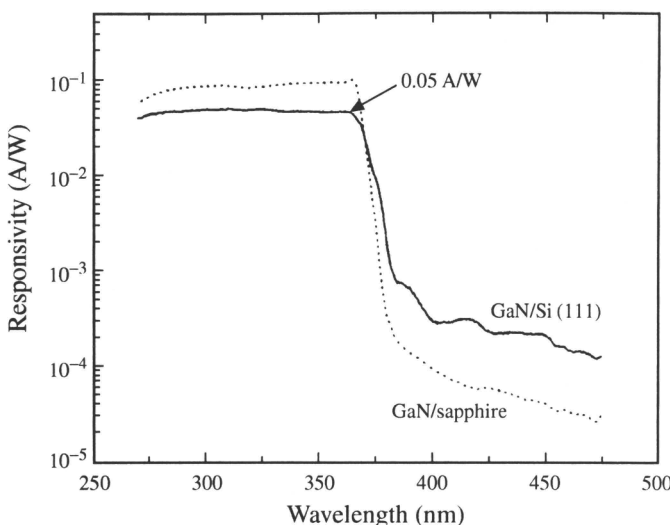


Figure 12.16 Comparison of the spectral response characteristics of Pd/GaN detectors ($200 \times 200 \mu\text{m}^2$) grown on Si(111) by MBE and on sapphire by MOVPE (after Ref. 93).

bandgap, with an abrupt cut-off which shifts to higher energy for increasing Al content. Both the spectral behavior and the maximum responsivity were found to be independent of diode size. The time response of these devices was RC -limited, with a minimum time response of 15 ns in devices with a diameter of $240 \mu\text{m}$.⁹⁰

Planar GaN Schottky photodiodes with an active area of $200 \times 200 \mu\text{m}^2$ have also been fabricated on Si(111).⁹³ Si is an attractive substrate for GaN because of its lower cost, well-developed technology, and the possibility of integrating $\text{Al}_x\text{Ga}_{1-x}\text{N}$ devices with Si-based integrated circuits. The spectral response of devices on Si(111) presents a sharp cut-off at 365 nm, with peak responsivities of 50 mA/W and a UV/visible contrast of about (see Figure 12.16). The enhanced response at wavelengths beyond the cut-off, compared with devices on sapphire, is likely a contribution of the substrate. Regarding the time response, a minimum decay time of 150 ns was measured in these devices.

In theory, the vertical structure makes it possible to achieve better quality Ohmic contacts, as they are deposited on a heavily doped layer, and higher responsivity and a lower capacitance, as the SCR is wider, because it is located in the undoped material. However, thus far better results have been obtained with lateral structures, which achieve higher speed, lower noise, and lower dark current. Simin and colleagues⁹⁴ attribute poorer results in vertical structures to the formation of surface defects during the mesa etching.

12.4.3 Time Response

In general, $\text{Al}_x\text{Ga}_{1-x}\text{N}$ -based Schottky photodiodes present exponential photocurrent decays, with a time constant which depends linearly on the load resistance,^{87,88,90,91,93} as shown in Figure 12.17. The devices are limited by the RC product of the system, where C is the diode capacitance, and R is the sum of the load resistance (R_L) and the diode series resistance (R_S). The device time constant increases with the Schottky contact area,^{90,91} because $C \propto A$, as expected. On the other hand, the application of reverse bias implies a reduction of the diode capacitance (see Eq. (12.47)). Because the series resistance does not depend on bias, the device time response decreases proportionally to $(\Psi_0 + V_B)^{-\frac{1}{2}}$. This behavior has been checked experimentally,^{91,93} as shown in Figure 12.18.

For planar devices with the same geometry, R_S and C are proportional to $(\mu N_D)^{-1}$ and $N_D^{-\frac{1}{2}}$, respectively, so that the bandwidth of these devices increases with $\mu N_D^{\frac{1}{2}}$. Provided that an increase in the mobility is observed for low n -type doping levels,^{63,95,96} a certain Si doping ($\lesssim 10^{18} \text{ cm}^{-3}$) improves the time response in planar devices.

12.4.4 Noise Performance

Although shot noise might become dominant at high frequencies,⁹³ $1/f$ noise has been measured to be dominant at low and medium frequencies in GaN and $\text{Al}_x\text{Ga}_{1-x}\text{N}$ Schottky photodiodes.^{87,88,90,93} Thus, the noise power

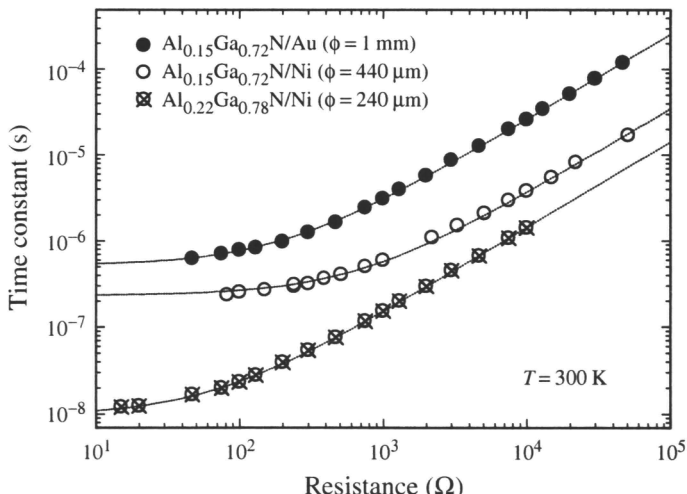


Figure 12.17 Photocurrent decay time as a function of load resistance. Lines correspond to linear fits. (after Ref. 90).

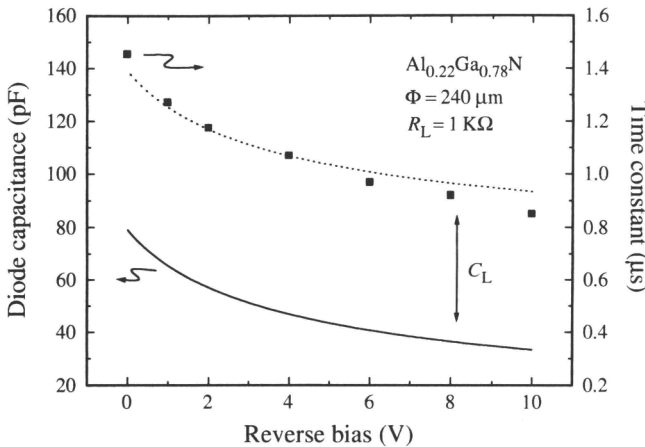


Figure 12.18 Variation of the device capacitance and the time constant of the photocurrent decays as a function of reverse bias. The dotted line represents the sum of the diode internal capacitance and the load capacitance, C_L . (After Ref. 91).

spectral density, S_n , is found to satisfy the relationship:

$$S_n = \frac{s_0 I_d^\alpha}{f^\gamma} \quad (12.51)$$

where I_d is the dark current, f is the frequency, and s_0 , γ , and α are dimensionless fitting parameters. Values of $0.94 \leq \gamma \leq 1.2$, and $1 < \alpha \leq 2$ have been found.

The NEP of these devices is obtained as:

$$\text{NEP} = \frac{\sqrt{\langle i_{shot}^2 \rangle + \langle i_{1/f}^2 \rangle}}{R_i} \quad (12.52)$$

where i_{shot} is the shot noise current, $i_{1/f}$ is the $1/f$ noise current, and R_i is the device responsivity. The value of $\langle i_{shot}^2 \rangle$ can be estimated by $\langle i_{shot}^2 \rangle = 2qI_d \text{BW}$, where BW is the photodiode bandwidth, whereas $\langle i_{1/f}^2 \rangle$ is obtained by integrating $S_n(f)$ over the bandwidth. An NEP normalized to the square root of the bandwidth of $8 \text{ pW}/\sqrt{\text{Hz}}$ and $41 \text{ pW}/\sqrt{\text{Hz}}$ have been obtained, respectively, in GaN/Au and Al_{0.22}Ga_{0.78}N/Au Schottky photodiodes, at -2 V bias.⁹⁰

The normalized detectivity, D^* , is the adequate parameter to compare different detectors:

$$D^* = \frac{\sqrt{A_{opt} \text{BW}}}{\text{NEP}} \quad (12.53)$$

where A_{opt} is the optical area of the device. Detectivities of $6.1 \times 10^9 \text{ W}^{-1} \text{ Hz}^{-\frac{1}{2}} \text{ cm}$ and $1.2 \times 10^9 \text{ W}^{-1} \text{ Hz}^{-\frac{1}{2}} \text{ cm}$ have been reported, respectively, in GaN/Au and Al_{0.22}Ga_{0.78}N/Au Schottky photodiodes, at -2 V bias.⁹⁰

12.4.5 Schottky Photodiodes on ELOG GaN

Despite the impressive development of III-nitride technology in the last decade, a high density of defects is still present in heteroepitaxial materials grown on sapphire ($> 5 \times 10^8 \text{ dislocation/cm}^2$). Light absorption by these defects produces a certain response to visible photons, which reduces the UV/visible contrast in GaN photodetectors.

Epitaxial lateral overgrowth (ELOG) is a promising technique to achieve quasi-defect-free GaN.^{97,98} This growth method has reduce the dislocation density in at least two orders of magnitude. The ELOG technique consists of growing GaN on a pattern of windows opened by photolithography in a dielectric layer (SiO₂, Si₃N₄) deposited on a GaN layer grown on sapphire or SiC. GaN nucleates in the windows and grows laterally, so that the propagation of threading dislocations is avoided over the masked area. Thus, a sequence of high-quality material (over the mask) and highly dislocated material (over the mask windows) is obtained. typical pattern consist of stripes, with a period of 10 to 20 μm . Therefore, a standard detector should cover both high-quality and low-quality material, with characteristics being an average of both.

There are three alternatives to avoid the low-quality regions over the openings of the mask:

- *Double ELOG*: Two dielectric layers with two photolithographic steps, the second pattern being complementary to the first one. Thus, defects are confined to the coalescence boundaries, but it is necessary to take the sample out of the growth chamber twice, and an extra photolithographic process.
- *Pendoepitaxy*⁹⁹: This approach differs from ELOG in the mask definition process, where both the dielectric layer and the GaN epitaxial layer are etched. The lateral growth starts below the dielectric mask until coalescence is achieved in the middle of the windows. Then regrowth continues until the layers coalesce over the mask. With this technique, dislocations are confined to the coalescence boundaries, in the middle of both the dielectric bands and the windows.
- *Two-step ELOG*¹⁰⁰: Once the dielectric has been deposited and patterned, during a first step standard growth conditions for GaN are

used, so that vertical growth rate is higher than the lateral growth rate. Under these conditions, there is a critical point at which threading dislocations bend by 90° and propagate horizontally until the coalescence boundary. Thus, the dislocation density is greatly reduced, although the surface presents peaks and valleys. Planarization is achieved in a second step, either by Mg-doping or by increasing the growth temperature, so that lateral growth rate is higher than vertical growth rate. With this technique, the dislocation density is reduced not only over the masked area but also over the openings of the mask. An average dislocation density of $5 \times 10^6 \text{ cm}^{-2}$ is achieved.

Semitransparent Au-Schottky barrier photodiodes have been fabricated on two-step ELOG GaN layers,¹⁰¹ showing a responsivity of 130 mA/W. An improvement of one order of magnitude in the UV/visible contrast has been observed, in contrast with devices on standard GaN on sapphire, as shown in Figure 12.19. The leakage current is significantly reduced, below 1 nA/cm² at -1 V bias. The device time response is RC -limited, and the lower residual doping in these layers increases the bandwidth to over 30 MHz, 12 MHz, and 8 MHz in devices with a diameter of 200 μm, 400 μm, and 600 μm, respectively. Normalized detectivities as high as $5 \times 10^{11} \text{ W}^{-1}\text{Hz}^{\frac{1}{2}}\text{cm}$ were measured at -3.4 V bias in Schottky photodiodes on two-step ELOG, with a diameter of 400 μm.

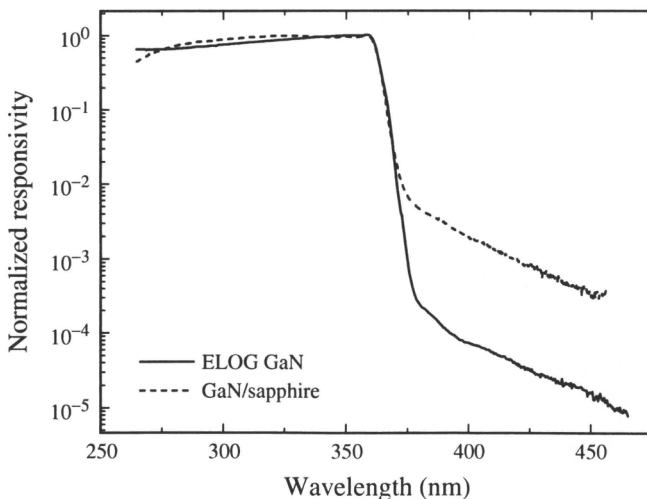


Figure 12.19 Spectral response of a Schottky photodiode fabricated on ELOG GaN, in comparison with a typical device on standard GaN on sapphire (after Ref. 101).

12.4.6 Schottky Photodiode as Biological UV Sensor

UV radiation is able to produce a number of biological effects:^{102–105}

- Skin pigmentation: maximum effect at 360 to 440 nm.
- Erythema (skin reddening): maximum at $\lambda < 297$ nm.
- Plant damage: $\lambda < 317$ nm.
- Bactericidal radiation: 210 to 310 nm; maximum at 254 nm.
- Carcinogenic radiation: UV-B and UV-C; maximum at 310 nm.
- DNA damage: $\lambda < 320$ nm, increasing rapidly for shorter wavelengths.
- Synthesis of vitamins D₂ and D₃: 249 to 315 nm; maximum at 290 nm.

Therefore, simple, accurate, reliable, low-cost instruments are required to evaluate the biological effects of UV radiation. Broad-band UV detectors have been developed to fit the erythema action of the UV-A and UV-B wavelengths.¹⁰² Commercial UV meters consist of narrow bandgap photodiodes (Si, GaAs, GaP), with a series of filters and phosphors in the optical path.¹⁰⁶

By using a certain Al mole fraction and proper growth conditions, Muñoz and coworkers¹⁰⁷ have demonstrated that the spectral response of Al_xGa_{1-x}N Schottky photodiodes can fit the erythema action spectrum, as shown in Figure 12.20. Thus, the responsivity of these devices provides direct and reliable information on the biological effects of UV radiation.

To monitor solar UV-B radiation and the solar UV radiation effects, Al_xGa_{1-x}N photodetectors offer design flexibility, low cost, minimal size, and no need for filters or coatings, nor for temperature stabilization chambers. These detectors are suitable to perform both narrow-band or broad-band irradiance measurements and to monitor biological hazards. GaN photodiodes have already been tested as solar UV-meters⁸⁹ with promising results (see Figure 12.21).

12.4.7 Schottky Photodiode Arrays

UV photodetector arrays would constitute the core of visible-blind cameras, expected to be used in many applications, such as flame detection, missile guidance, and astrophysics studies. To achieve high performance, good homogeneity and reduced crosstalk between pixels are required.

The fabrication of an 8 × 8 Schottky barrier photodiode array on GaN with pixel size of 200 × 200 μm², has been reported.¹⁰⁸ This array shows an average peak responsivity of 46 mA/W with a deviation of 1.91 percent, and an average dark current of 20 nA at –1 V. The time response is ~50 ns

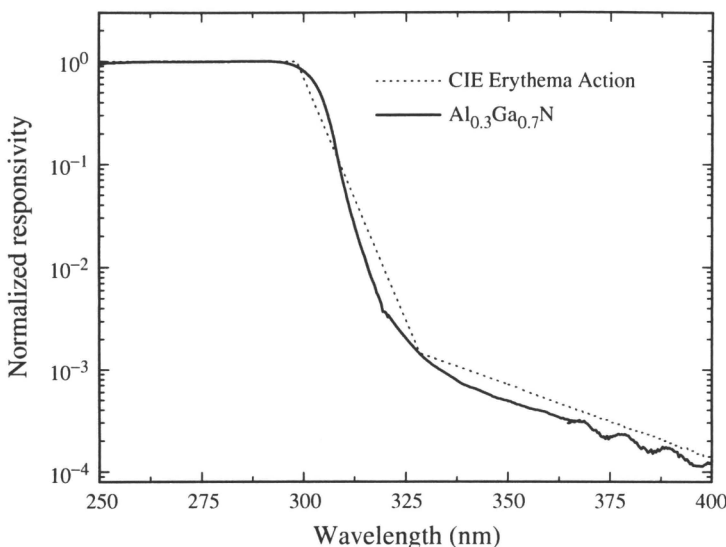


Figure 12.20 Spectral response of an AlGaN Shottky photodiode, compared with the CIE erythema action spectrum.

on $50\ \Omega$. For pixels that are not in the same row or column as the illuminated pixel, the crosstalk was approximately -62 dB . However, for pixels in the same row and column, crosstalk increases to -38 dB , due to the reverse leakage currents in the common metal lines.

12.5 METAL-SEMICONDUCTOR-METAL (MSM) PHOTODIODES

MSM photodiodes are an attractive choice for UV detectors, given their fabrication simplicity, low dark current, and high bandwidth capability.^{4,6} The lateral, planar structure of these devices results in an extremely low capacitance, which matches well the requirements of high-speed performance. On the other hand, the fabrication process for MSM photodiodes is compatible with field effect transistors, which makes them suitable for integration in an optical receiver.¹⁰⁹

12.5.1 General Principles

MSM devices consist of a photoabsorbing semiconductor layer with two interdigitated Schottky contacts deposited on top. Thus, the difficulty of achieving good Ohmic contacts on high-Al-content material is avoided. For their operation, the devices are biased with a voltage

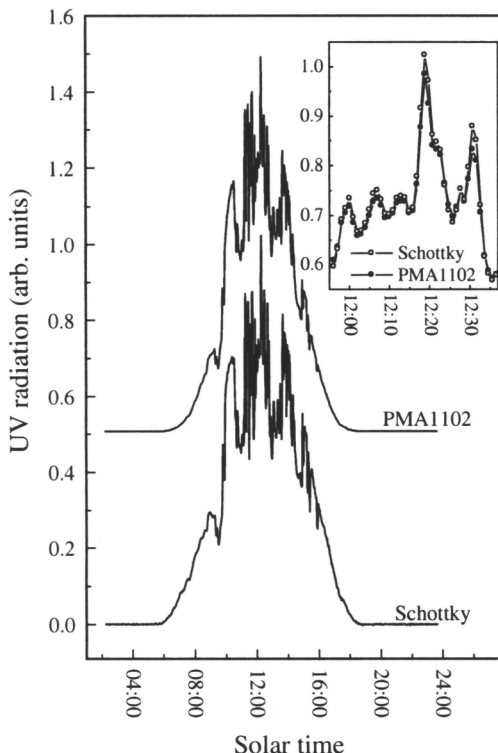


Figure 12.21 Normalized solar-UV measurements on a sunny day with some traveling clouds, recorded both with a GaN Schottky photodetector and by the commercial instrument PMA1102 (vertically shifted for clarity). On an expanded scale, the inset shows the UV data during a short period of time. (After Ref. 89).

source and connected in series with a current amplifier, as depicted in Figure 12.22.

12.5.1.1 Band diagram

A detailed analysis of the potential distribution in MSM structures can be found in Sze and colleagues.¹¹⁰ When bias is applied, one of the Schottky contacts (A) is reverse biased (cathode), whereas the other (B) is forward biased (anode), as shown in Figure 12.23a. The sum of the two Schottky barrier-related SCRs increases with bias. At a certain voltage, named reach-through voltage, V_{RT} , the SCRs cover all the distance between contacts, as shown in Figure 12.23b. For even higher bias ($V_B = V_{FB}$, flat-band voltage), the electric field in $x = L$ is canceled, so that the energy bands become flat (Figure 12.23c). For bias greater than V_{FB} , the energy bands bend even more,

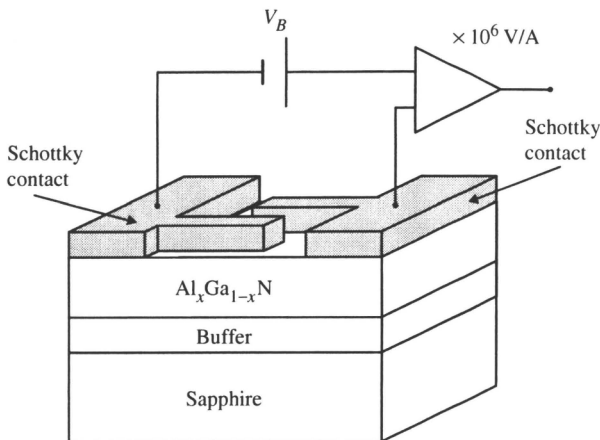


Figure 12.22 Schematic diagram and measuring circuit of a MSM photodiode.

as shown in Figure 12.23d. The maximum bias is limited by avalanche breakdown at the semiconductor point where the electric field is more intense, near the A contact.

In a symmetric MSM structure (both contacts with the same area and barrier height), V_{FB} is given by:¹¹⁰

$$V_{FB} = \frac{q N_D L^2}{2 \epsilon_s \epsilon_0} \quad (12.54)$$

and the reach-through voltage, V_{RT} , is obtained as:

$$V_{RT} = \frac{q N_D L^2}{2 \epsilon_s \epsilon_0} - 2\Psi_0 = V_{FB} - 2\Psi_0 \quad (12.55)$$

12.5.1.2 Responsivity

In an ideal MSM photodiode, there is no internal gain, because the Schottky barriers prevent the injection of majority carriers. The current across the device should only be due to the photogenerated electron hole pairs, drifted by the intense electric field. Thus, the responsivity is given by Eq. (12.2) with $g = 1$.

In real devices, electrons may cross the potential barriers by thermionic field emission, producing a leakage current, which is subject to the same gain mechanism previously described in photoconductive devices. This gain can seriously deteriorate the performance at low frequencies and even introduce persistent photoconductivity effects.

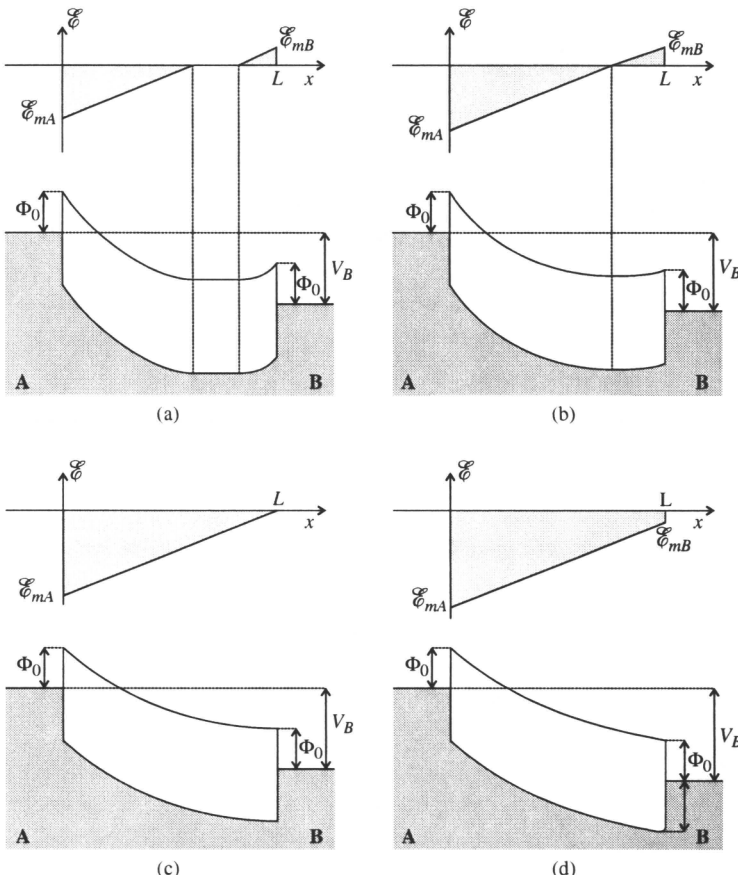


Figure 12.23 Electric field distribution, $E(x)$, and energy band diagram of a MSM photodiode at a bias voltage, V_B , such that (a) $V_B < V_{RT}$; (b) $V_B = V_{RT}$; (c) $V_B = V_{FB}$; (d) $V_B > V_{FB}$.

12.5.1.3 Time response

The time response of MSM photodiodes can be limited by a number of factors, such as:

- RC constant, due to parasitic impedances linked to the geometric structure,
- transit time between fingers, and
- low-frequency gain related phenomena.

Regarding parasitic impedances, the simplest model of an MSM photodiode consists of a current source in parallel with the device capacitance.

A detailed analysis of the capacitance of these structures was presented by Lim and Moore.¹¹¹ A simple but precise enough approximation is generally used for device design:¹¹²

$$C = \frac{A\epsilon_0(\epsilon_s + \epsilon_p)}{L + d} \frac{\pi}{4Ln(8/\pi + L/d)} \quad (12.56)$$

where A is the interdigitated area, ϵ_0 is the vacuum permittivity, ϵ_s and ϵ_p are the dielectric constants of the semiconductor and the passivation layer, and L and d are the gap spacing and the finger width, respectively. Only if the device has to operate at microwave frequencies is it necessary to turn to more complex models, analyzing the fingers as transmission lines.¹¹³

In general, in devices having no low-frequency gain problems and working on low load resistances ($\sim 50 \Omega$), the speed is limited by the transit time, given by:

$$t_t = \frac{L}{v_{sat}} \quad (12.57)$$

where v_{sat} is the carrier saturation velocity.

12.5.2 Current-Voltage Characteristic

The two Schottky barriers behave as obstacles for carrier transport, so that extremely low dark currents are measured in MSM photodiodes. Dark currents of ~ 350 fA at 10 V bias have been measured for GaN MSM photodiodes with an interdigitated area of $250 \times 250 \mu\text{m}^2$.¹¹⁴ The thermionic emission is the dominant current mechanism in some devices, whereas an enhancement of the thermionic field emission current is observed in large area structures¹¹⁴ or in devices fabricated on thin GaN layers ($\sim 1.5 \mu\text{m}$).¹¹⁵

The current-voltage characteristics of some GaN MSM photodiodes presents a punch-through effect,¹¹⁵ characterized by a sudden increase in the dark current (usually two to three orders of magnitude) over a very narrow voltage range (typically < 3 V). The punch-through voltage decreases with the residual doping level and shows no dependence on the electrode gap spacing.

Depletion region reach-through could introduce such behavior in the dark current. However, due to the residual doping ($\sim 6 \times 10^{16} \text{ cm}^{-3}$) in GaN layers, high voltages are required to achieve reach-through with reasonable electrode gap spacings ($> 1 \mu\text{m}$), according to Eq. (12.55). Therefore, in all the devices analyzed, the band diagram corresponds to Figure 12.23a. On the other hand, the fact that the punch-through voltage does not depend on electrode pitch discards that reach-through cannot be responsible for the current increase.

Carrano and co-authors¹¹⁵ explain the punch-through effect as due to the high residual doping in the buffer layer. When bias is applied, the cathode SCR grows until it reaches the buffer layer, where it stacks, due to the high doping concentration. A two-dimensional computer simulation of the device under bias predicts punch-through voltages that correlate quite well with experimental results. This explanation justifies that the punch-through effect is not observed in devices on thick GaN layers ($>2\text{ }\mu\text{m}$).

12.5.3 Responsivity

12.5.3.1 Linearity and spectral response

$\text{Al}_x\text{Ga}_{1-x}\text{N}$ MSM photodiodes behave linearly, with optical power for excitation both above and below the bandgap (see Figure 12.24) and independently of bias.¹¹⁶ This dependence proves the absence of the gain mechanism dominant in $\text{Al}_x\text{Ga}_{1-x}\text{N}$ photoconductors^{15,36} described previously, and confirms the high quality of the Schottky contacts.

The spectral response for $\text{Al}_x\text{Ga}_{1-x}\text{N}$ MSM photodiodes is shown in Figure 12.25.¹¹⁷ The responsivity is quite flat above the bandgap and presents a sharp cut-off, with a UV/visible contrast of more than four decades at high bias ($V_B \geq 5\text{ V}$).^{115–118} At lower bias, a reduction of the visible rejection is observed.¹¹⁴

As discussed previously, a low doping level is required in order to achieve reach-through with reasonable electrode gap spacings. An approach for

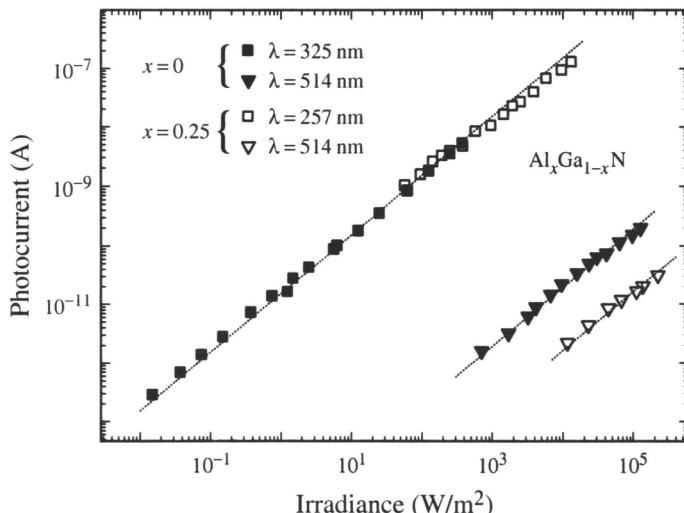


Figure 12.24 Photocurrent dependence on optical power for $\text{Al}_{0.25}\text{Ga}_{0.75}\text{N}$ and GaN MSM photodiodes, measured over and below the bandgap (after Ref. 116).

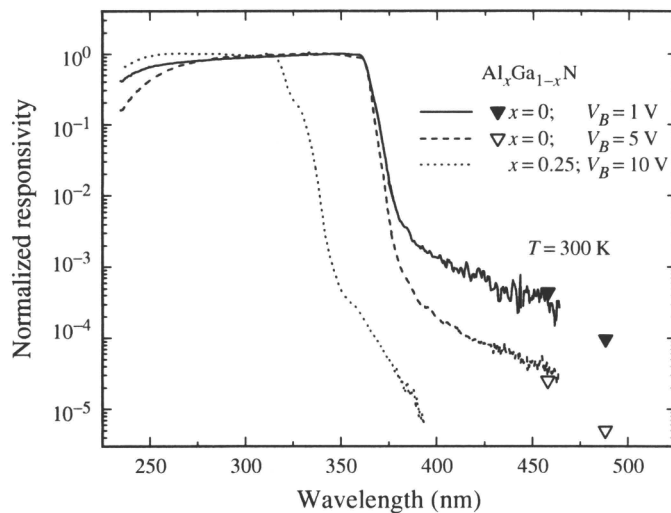


Figure 12.25 Spectral response of $\text{Al}_{0.25}\text{Ga}_{0.75}\text{N}$ and GaN MSM photodiodes, measured at different bias (after Ref. 117).

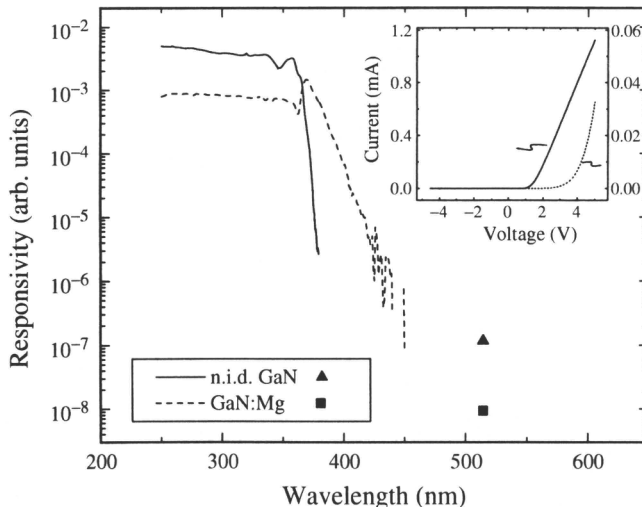


Figure 12.26 Spectral response of n.i.d. GaN and GaN:Mg MSM photodiodes. In the inset, I - V characterization of the Schottky contacts. (after Ref. 118).

decreasing the carrier concentration consists of compensating the sample by means of Mg-doping.⁶⁸ However, Mg introduces some secondary effects on devices, as shown in Figure 12.26. Undoped GaN detectors show a very abrupt cut-off, whereas the GaN:Mg MSM detector presents a more gradual

decline at longer wavelengths.¹¹⁸ This slight absorption of photons with energy below the bandgap is due to the depth of Mg-related levels.

12.5.3.2 Bias dependence

Regarding the variation of responsivity with bias, a superlinear behavior is observed in most cases, for $V_B > 1\text{ V}$.^{114,116,118,119} Monroy and colleagues¹¹⁴ also report a sublinear dependence of the responsivity on bias for $V_B < 2\text{ V}$, as shown in Figure 12.27a, which fits well with a one-dimensional model of MSM photodiodes in absence of gain (dashed line in Figure 12.27a). An abrupt increase of the responsivity is observed between 2 V and 5 V, indicative of a bias-activated gain mechanism, which saturates at higher bias. This behavior is independent of finger width and gap spacing.

For the present residual doping concentration, barrier height, and device geometry, the reach-through voltage of these MSM structures should be higher than 200 V, even for devices with a pitch of 2 μm . Thus, most of the applied bias voltage drops in the cathode, and the photocurrent is produced by light absorption in the cathode SCR, with a small negative contribution from the anode region. The higher responsivities observed in devices with shorter gap spacing¹¹⁴ are not due to a more intense electric field, but to a higher number of fingers in the illuminated region, which implies a larger cathode SCR, proportional to the contact perimeter.

The gain mechanism observed in these devices is also wavelength-dependent, as shown in Figure 12.27b. For wavelengths longer than the bandgap, the device follows the trend expected for a MSM photodiode in absence of gain. The deviation from this behavior appears only for wavelengths shorter than 370 nm, so that the enhancement of the visible rejection with bias and gain are due to the same mechanism.

The presence of gain in GaN photodetectors is usually related to slow photoconductivity phenomena. However, these devices present exponential photocurrent decays, with time constants corresponding to the RC product of the measuring system, independent of bias. Moreover, the variation of the photocurrent time response with the load resistance presents no trace of saturation for low load resistances.¹¹⁶

Gain in interdigitated MSM photodiodes has been reported and attributed to different mechanisms.^{120–122} The most often suggested process consists in electron tunneling enhanced by hole accumulation at the cathode. This accumulation may be due to traps located either at the semiconductor surface in the bulk material, or in a thin insulating layer between the metal and the semiconductor. Trapping at surface states or dislocations produces persistent photoconductivity effects and a sublinear behavior with optical power, and degrades the spectral response of the devices. Both the linearity and the fast response of MSM photodiodes prove the absence of this gain mechanism,

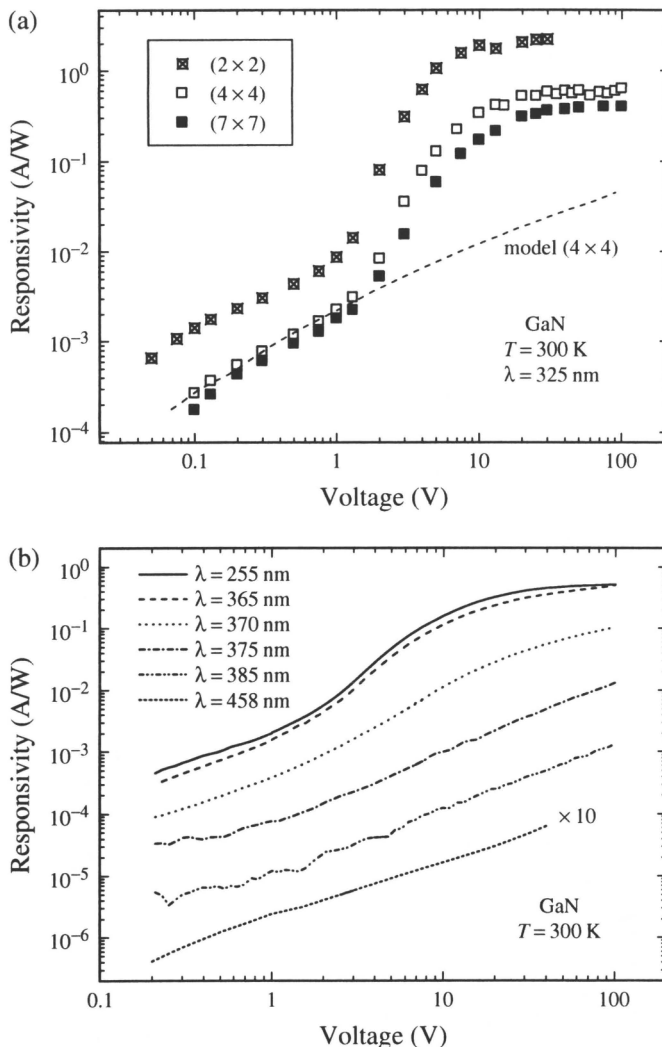


Figure 12.27 Responsivity dependence on bias in GaN MSM photodiodes (a) for excitation over the bandgap ($\lambda = 325$ nm) in diodes with finger width and gap spacing of 2, 4, and 7 μm , and with a $250 \times 250 \mu\text{m}^2$ interdigitated area; (b) for different excitation wavelengths (after Ref. 114).

which is dominant in GaN and $\text{Al}_x\text{Ga}_{1-x}\text{N}$ photoconductors.^{15,36} The presence of deep hole traps in bulk n.i.d. GaN is responsible for the photoresponse at excitation wavelengths longer than the bandgap, but the fact that gain is not observed for $\lambda > 370$ nm rules out trapping at these levels as the origin of this gain.

The increase in hole density in the vicinity of the cathode can also be explained by the difference in transit speeds between electrons and holes.¹²⁰ However, this phenomenon cannot justify a gain which is active only for wavelengths above the bandgap. Finally, we can speculate about an avalanche process in the valence band as responsible for the gain. At high bias, holes generated in the valence band near the cathode move toward the contact driven by the intense electric field, and might have enough energy to provoke new transitions by impact-ionization. Further experimental and theoretical research is required to determine the physical origin of the gain in present MSM photodiodes.

A responsivity independent of bias has been reported in GaN MSM devices.¹²³ Given the residual doping level of the layer ($6 \times 10^{16} \text{ cm}^{-3}$) and the gap spacing (2 μm), reach-through is not expected in these devices. However, considering the high responsivity, it is possible that a long diffusion length compensates the narrowness of the SCRs.

12.5.4 Time Response

MSM photodiodes are specially suitable for high-speed applications. Given their intrinsically low capacitance, the time response of MSM photodiodes is usually limited by the carrier transit time. A bandwidth in excess of 1 GHz has been observed in GaN MSM photodiodes with a gap spacing of 2 μm and an interdigitated area of $50 \times 50 \mu\text{m}^2$.¹²⁴

Mg-doping was also proved to affect the time response of MSM photodiodes.¹¹⁸ Doped devices exhibit exponential photocurrent decays for high load resistances ($> 50 \text{ k}\Omega$), but they become nonexponential, and finally saturate, for lower load resistances. A minimum time response of 200 ns was obtained in devices with a gap spacing of 10 μm .¹¹⁸

The time response of GaN MSM photodiodes can be further improved by optimizing the device geometry. Theoretical studies predict a bandwidth over 100 GHz for 0.25- μm GaN MSM photodiodes at 3.75 V bias,¹²⁵ and further improvements could be achieved by operating the device at high electric fields, in the ballistic regime. The use of graded $\text{Al}_x\text{Ga}_{1-x}\text{N}$ layers has also been proposed¹²⁶ in order to increase the detector bandwidth. The advantage of this structure arises from the capability of rapid hole removal facilitated by the presence of a built-in electric field.

12.5.5 Noise Performance

Extremely low noise levels have been achieved in $\text{Al}_x\text{Ga}_{1-x}\text{N}$ MSM photodiodes under dark conditions. For GaN photodiodes, the noise power spectral density remains below the noise background of the measuring system ($10^{-26} \text{ A}^2/\text{Hz}$) up to 28 V bias for all the geometries under study.^{114,127} This result implies a normalized NEP* lower than $2 \text{ pW}/\text{Hz}^{\frac{1}{2}}$ at 28 V

bias in devices with finger width and pitch of 2 μm and an interdigitated area of $250 \times 250 \mu\text{m}^2$.¹¹⁴ At this bias, 1/f noise have been observed in Al_{0.25}Ga_{0.75}N MSM photodiodes at low frequencies. From this measurement, an NEP* of $\sim 24 \text{ pW/Hz}^{1/2}$ is calculated for devices with a finger width of 7 μm and a gap spacing of 12 μm in an interdigitated area of $1 \times 3 \text{ mm}^2$.¹²⁷

12.5.6 MSM Photodiodes on ELOG GaN

MSM photodiodes fabricated on ELOG GaN on sapphire have been reported.¹²⁸ Devices with fingers parallel to the dielectric (SiO₂) stripes showed better performance than those perpendicular to the pattern. The best detectors present high responsivity ($\sim 84 \text{ A/W}$), with a sharp cut-off at about 365 nm. However, the responsivity is related to photoconductive gain, as proved by the strong sublinear behavior of the photocurrent with incident power and the linear increase of the responsivity with bias. Time responses as low as 10 ns are reported for very high laser excitation power ($> 10^{11} \text{ W/m}^2$), but persistent photoconductivity is still dominant.

12.6 p-n AND p-i-n PHOTODIODES

Since the first reported GaN p-n junction photodiodes,^{86,129} which were limited by the quality of their p-type layer and contact, design and technology have evolved to make possible fast-response ($\tau \sim 105 \text{ ns}$)¹³⁰ and low-noise (NEP $\sim 61 \text{ fW/Hz}^{1/2}$ at -3 V bias)¹³¹ GaN p-n junctions. The performance of these devices have been further improved by introducing an intrinsic region (p-i-n diodes)¹³²⁻¹³⁵ and by using AlGaN/GaN heterostructures.¹³⁶⁻¹³⁸ A 32 \times 32 array of Al_{0.2}Ga_{0.8}N/GaN heterostructure p-i-n photodiodes has recently been presented.¹³⁹

12.6.1 General Principles

The p-n and p-i-n photodiodes are the most commonly used photovoltaic structures for radiation detection in the visible and infrared regions of the spectrum. Electrons and holes photogenerated in the SCR, or within a diffusion length, are separated by the intense electric field. Thus, a photocurrent is generated, proportional to the incident photon flux.

12.6.1.1 Responsivity

The responsivity is obtained as

$$R_i = \frac{q\eta\lambda}{hc} \quad (12.58)$$

where q is the electron charge, η is the quantum efficiency, and hc/λ is the photon energy.

In a p-n junction, the quantum efficiency, η , is the sum of the quantum efficiencies in the *p*-type, *n*-type, and space charge regions. In the *n*-type and *p*-type regions, minority carriers should diffuse toward the junction. Thus, illumination through the *p*-type layer is desirable to achieve a better minority carrier collection in that layer, because the diffusion length is longer for electrons. Assuming illumination through the *p*-type layer (see Figure 12.28), and a heavily doped *n*-type layer long enough to neglect surface recombination, the quantum efficiency is given by:

$$\eta = \eta_p + \eta_{SCR} + \eta_n \quad (12.59)$$

being

$$\begin{aligned} \eta_p &= \frac{(1-r)\alpha L_e}{\alpha^2 L_e^2 - 1} \\ &\times \left\{ \frac{\alpha L_e + \gamma - \left[\gamma ch\left(\frac{x_j - x_{SCR}}{L_e}\right) + sh\left(\frac{x_j - x_{SCR}}{L_e}\right) \right] e^{-\alpha(x_j - x_{SCR})}}{\gamma sh\left(\frac{x_j - x_{SCR}}{L_e}\right) + ch\left(\frac{x_j - x_{SCR}}{L_e}\right)} \right. \\ &\left. - \alpha L_e e^{-\alpha(x_j - x_{SCR})} \right\} \end{aligned} \quad (12.60)$$

$$\eta_{SCR} = (1-r)[e^{-\alpha(x_j - x_{SCR})} - e^{-\alpha x_j}] \quad (12.61)$$

$$\eta_n = \frac{(1-r)\alpha L_h(\alpha L_h - 1)}{\alpha^2 L_h^2 - 1} e^{-\alpha x_j} \quad (12.62)$$

where α is the absorption coefficient, x_j is the junction depth, x_{SCR} is the SCR width, L_e and L_h are the minority diffusion lengths, and γ is given by

$$\gamma = \frac{s_p L_e}{D_e} \quad (12.63)$$

where s_p is the surface recombination rate in the *p* region, and D_e is the electron (minority) diffusion coefficient.

12.6.1.2 Time response

The time response of these devices can be limited by three mechanisms:

- Diffusion time of carriers towards the SCR, t_{dif} , which is estimated as

$$t_{dif} \sim \frac{x_j^2}{D_{min}} \quad (12.64)$$

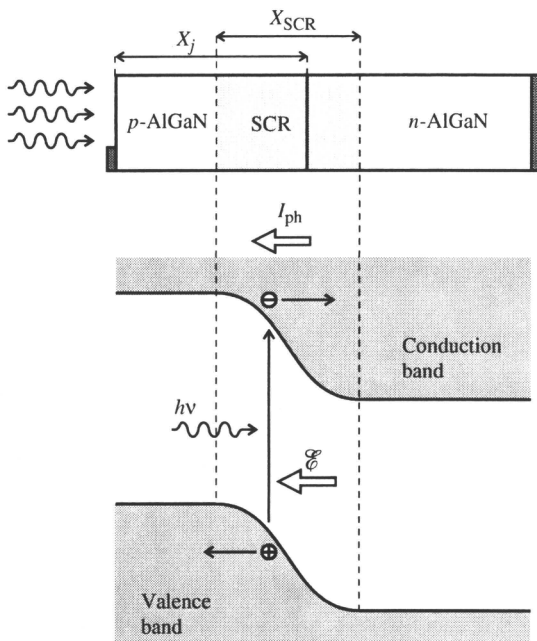


Figure 12.28 Schematic diagram of a p-n junction photodiode.

where x_j is the junction depth, and D_{min} is the minority diffusion coefficient.

- SCR transit time, $t_{t\text{SCR}}$, which is given by

$$t_{t\text{SCR}} = \frac{x_{\text{SCR}}}{v_{sat}} \quad (12.65)$$

where v_{sat} is the electron saturation velocity.

- RC constant, where R is the diode shunt resistance in parallel with the load resistance, and C is the junction capacitance.

Generally in a p-n junction, both the diffusion time and the transit time are negligible compared with the RC constant. In a p-i-n junction, however, the transit time can be higher than the RC , because the device capacitance is lower and the SCR is much wider.

12.6.1.3 Noise

The theory described above for Schottky photodiodes is directly applicable to p-n junction diodes. There are basically three noise components: $1/f$ noise, shot noise, and thermal noise, due to the device series resistance. In general,

shot noise is dominant at high frequencies, whereas at $1/f$ noise can be higher at low frequencies. As in Schottky photodiodes, thermal noise is usually negligible, compared with the other noise sources.

12.6.2 Responsivity

In $\text{Al}_x\text{Ga}_{1-x}\text{N}$ p-n and p-i-n photodiodes, photocurrent scales linearly with optical power over more than five decades.^{130,133,140,141} Typical zero-bias responsivity in a p-n or p-i-n homojunction GaN device lies in the range of 100 to 150 mA/W, corresponding to external quantum efficiencies of 30 percent to 40 percent. These results are improved by using $\text{Al}_x\text{Ga}_{1-x}\text{N}$ in the illuminated layer (either *n*-type or *p*-type), so that 365 nm photons are absorbed directly in the junction, thus avoiding diffusion losses. A responsivity as high as 200 mA/W at 365 nm has been reported for a sapphire-Al_{0.28}Ga_{0.72}N(n)-GaN(i)-GaN(p) heterostructure, illuminating through the substrate.¹³⁸

A decrease of the responsivity has been observed in $\text{Al}_x\text{Ga}_{1-x}\text{N}$ homojunctions when increasing the Al mole fraction of the ternary alloy,¹⁴⁰ probably due to the lower diffusion length of the layers. A maximum responsivity of 57 mA/W at 287 nm has been reported, which corresponds to a quantum efficiency of 25 percent.¹⁴²

An increase of the responsivity with bias was reported in all cases.^{131,134,136,138,140,141} This result confirms that the response is limited by carrier diffusion length. When the bias increases, the SCR broadens, so that carriers that are photoionized farther from the junction are collected.

Figure 12.29 shows typical spectral response of $\text{Al}_x\text{Ga}_{1-x}\text{N}$ p-i-n photodiodes with different Al contents. The responsivity is quite flat for photon energies above the bandgap. The cut-off shifts to shorter wavelengths and becomes less sharp for increasing Al content. A visible rejection of more than four orders of magnitude is obtained in all the devices. An Ar⁺ laser was used to check the visible-blindness of the devices, obtaining the data at 514 nm in Figure 12.29.

The low carrier diffusion length can affect the above-bandgap spectral response of $\text{Al}_x\text{Ga}_{1-x}\text{N}$ photodiodes.^{86,131,130,136} The absorption coefficient increases for shorter wavelengths, so that the absorption occurs close to the surface, that is, electron-hole pairs are generated farther from the junction in the top layer and must diffuse before collection. A short diffusion length results in a reduction of the responsivity for shorter wavelengths, which is more important for thicker top layers, as shown in Figure 12.30.

III-Nitride detectors provide a sharp long-wavelength cut-off, which is directly related to the bandgap of the material in the active region. For some applications, however, an additional short-wavelength cut-off, defining a UV band, is also required. In a theoretical study, Pulfrey and Nener¹⁴³

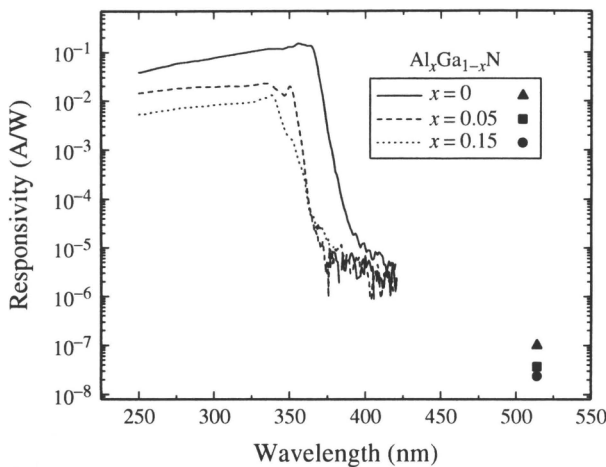


Figure 12.29 Zero-bias spectral response of $\text{Al}_x\text{Ga}_{1-x}\text{N}$ p-i-n photodiodes (after Ref. 140).

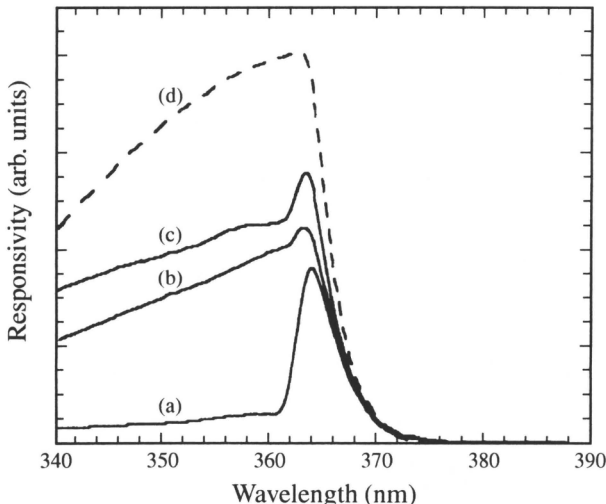


Figure 12.30 Zero-bias spectral response for GaN p-i-n photodetectors (a) with $0.2 \mu\text{m}$ p-layer, (b) with $0.1 \mu\text{m}$ p-layer, (c) with no p-layer except under the contact, and (d) an $\text{Al}_{0.12}\text{Ga}_{0.88}\text{N(p)-GaN(i)-GaN(n)}$ detector (- - -) (after Ref. 136).

pointed to the possibility of using $\text{Al}_x\text{Ga}_{1-x}\text{N}/\text{GaN}$ p-i-n heterostructures as UV-band detectors with a short-wavelength cut-off which corresponds to the $\text{Al}_x\text{Ga}_{1-x}\text{N}$ bandgap. The $\text{Al}_x\text{Ga}_{1-x}\text{N}$ layer should be thick enough so that it not only enhances the peak responsivity but also works as an integrated

short-pass filter. Devices with a 1- μm -thick $\text{Al}_{0.1}\text{Ga}_{0.9}\text{N}$ layer¹³⁷ and a 1.5- μm -thick $\text{Al}_{0.28}\text{Ga}_{0.72}\text{N}$ layer¹³⁸ have been demonstrated to achieve a short-wavelength rejection of more than two decades.

12.6.3 Time Response

RC-limited GaN p-n and p-i-n photodiodes have been reported,^{130,131} showing exponential photocurrent decays. At zero-bias, minimum time constants of about 27 ns have been measured in $200 \times 200 \mu\text{m}^2$ devices,¹³¹ decreasing to 11 ns at -6 V bias, due to the reduction of the junction capacitance with bias. Faster time responses (12 ns at zero bias) are obtained in AlGaN/GaN heterojunctions with a diameter of 250 μm .¹³⁶

However, photocurrent decays in these devices are often nonexponential, with minimum decay times higher than expected for an RC limitation.^{129,132,133,140} A correlation between this behavior and the variation of the device capacitance with frequency has been reported.¹⁴⁰ The capacitance shows a step at a certain frequency, which increases with temperature. In all cases, time response was found to decrease with reverse bias, corresponding to capacitance limited devices.^{129–131,133,135}

This behavior indicates the presence of a defect level in the semiconductor, which cannot react to excitation over a certain frequency. The thermal activation energy of the defect was estimated to be 99 meV¹⁴⁰ from admittance spectroscopy measurements.¹⁴⁴ Taking into account this low activation energy and the high defect concentration ($\sim 1.5 \times 10^{18} \text{ cm}^{-3}$), obtained from capacitance versus voltage measurements at low frequency, it is concluded that the defect is most probably substitutional Mg. However, the value of 99 meV is low compared with the 150 meV thermal activation of Mg found by Hall measurements.¹⁴⁵ A similar capacitive behavior has been observed by Zohta and co-authors¹⁴⁶ in blue and green LEDs.

Very-high-speed GaN p-i-n photodiodes have been reported by Carrano and colleagues,^{124,135} with decay times below 1 ns at -5 V bias. This result was obtained by increasing the i-layer thickness to 1 μm , so that the device shows an extremely low capacitance. Therefore, the RC product no longer limits the time response and the devices are transit-time limited. The only drawback of this design is the low responsivity, below 30 mA/W at -5 V bias. Such devices working at high reverse bias are ideal for very-high-speed detection.

12.6.4 Noise

A detailed characterization of the noise performance of GaN p-n junction photodetectors was presented by Kuksenkov and coworkers.¹⁴⁷ At elevated

temperatures or high values of the reverse bias, where the dark current of the photodiode increases above ~ 1 nA, the appearance of $1/f$ noise is observed, satisfying the equation:

$$S_n = \frac{s_0 I_d^2}{f^\gamma} \quad (12.66)$$

where S_n is the noise power spectral density, I_d is the dark current, f is the frequency, and s_0 and γ are dimensionless constants. The value of γ is found to vary from 1.0 to 1.1. The parameter s_0 decreases slightly with increasing bias and rapidly with increasing temperature.

From the exponential variation of the dark current with both current and temperature, Kuksenkov and colleagues⁴⁷ conclude that the current is due to hopping of carriers via localized defect-related states (traps) in the depletion region. According to this, $1/f$ noise is explained as due to the presence of localized states separated from each other by distances longer than the typical electron jump length. Such sites are not incorporated into the conducting trap network, but slowly exchange electrons with those conducting traps, leading to fluctuations in the total number of electrons taking part in hopping conduction. This model, called the number fluctuation theory,¹⁴⁸ explains a frequency dependence of the noise spectral density given by the Hooge formula⁹:

$$S_n = \alpha \frac{I_d^2}{f \bar{N}} \quad (12.67)$$

where α is the Hooge parameter, and \bar{N} is the average number of electrons taking part in the conduction process. Fitting the experimental results to this equation, Kuksenkov and colleagues⁴⁷ obtain $\alpha \approx 3$ and $\bar{N} \approx 2.3 \times 10^5$. The increase of $s_0 = \alpha/\bar{N}$ with bias is explained by the increase of \bar{N} due to the broadening of the SCR, and the increase of s_0 with temperature is due to the increasing length of a typical jump.

Noise performance was also characterized under forward bias.¹⁴⁷ In these conditions, the built-in electric field decreases and hopping is no longer a dominant transport mechanism, but current is dominated by carrier diffusion in the neutral region. Thus, $1/f$ noise is not observed, and most of the devices show a clear generation-recombination noise component, with a Lorentzian spectrum. From an Arrhenius plot of the peak frequency versus temperature, Kuksenkov and colleagues calculate an activation energy of 490 meV, which is speculated to be due to Ga antisite defects.¹⁴⁹

Under illumination at reverse bias, the noise spectral density was flat at high frequencies, showing a good fitting to the $S_n = 2q I_{ph}$ value expected from the shot noise theory.

A noise equivalent power as low as $6.6 \text{ fW}/\text{Hz}^{\frac{1}{2}}$ has been obtained in p-n junction photodiodes at -3 V bias.^{131,147} These devices presented an optical area of $200 \times 200 \mu\text{m}$, so that the normalized detectivity is as high as $3 \times 10^{12} \text{ W}^{-1} \text{ Hz}^{\frac{1}{2}} \text{ cm}$.

12.6.5 p-i-n Photodiodes on ELOG GaN

$\text{Al}_{0.33}\text{Ga}_{0.77}\text{N}$ p-i-n photodiodes on ELOG GaN have recently been reported.¹⁴² The devices were fabricated on standard ELOG, with an SiO_2 mask consisting of $35\text{-}\mu\text{m}$ -wide stripes with $5\text{-}\mu\text{m}$ openings. The $10\text{-}\mu\text{m} \times 100\text{-}\mu\text{m}$ diode mesas were contained within the laterally overgrown wings. For comparison, additional devices with $30\text{-}\mu\text{m} \times 100\text{-}\mu\text{m}$ mesas were fabricated, so that they also spanned the coalescence region between two ELOG wings. Finally, similar devices with $300\text{-}\mu\text{m} \times 300\text{-}\mu\text{m}$ square mesas were fabricated on standard GaN on sapphire.

Leakage current densities as low as $10 \text{ nA}/\text{cm}^2$ at -5 V are measured in “wing” devices, one order of magnitude lower than in devices that also spanned the coalescence region, and more than six decades lower than in devices on standard GaN on sapphire (see Figure 12.31). This huge decrease in the leakage current is due to the much reduced dislocation density,

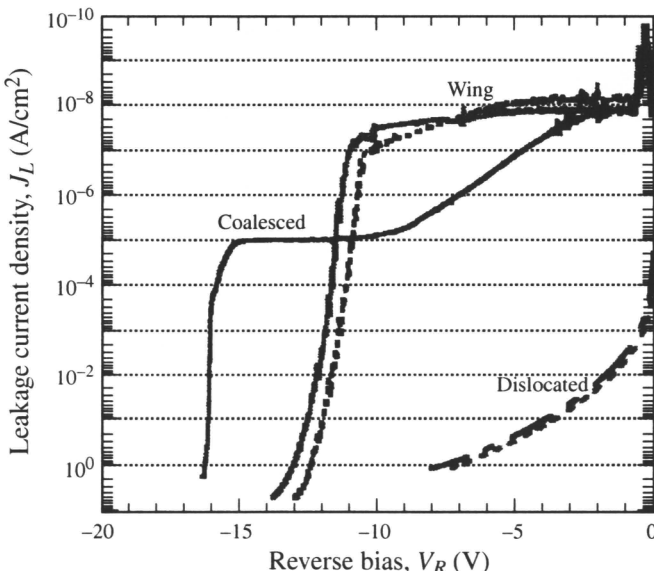


Figure 12.31 Typical dark current densities for p-i-n diodes fabricated on the wing region of the ELOG GaN, on the wing region including the coalescence boundary, and on dislocated GaN (after Ref. 142).

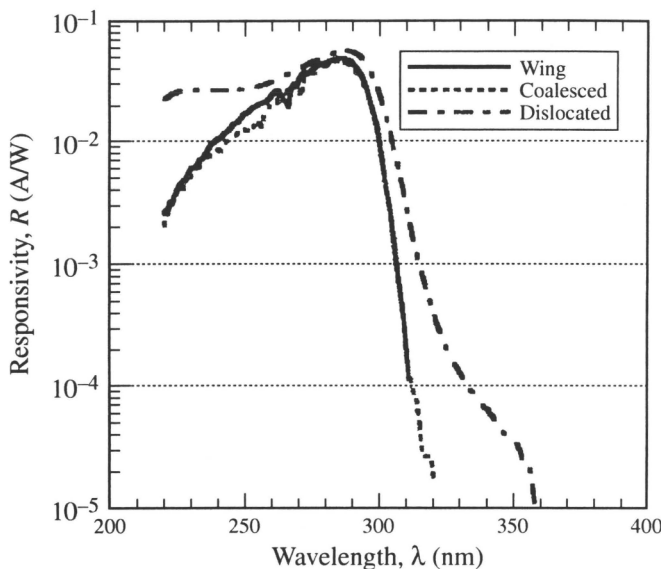


Figure 12.32 Spectral response for p-i-n diodes fabricated on the wing region of the ELOG GaN, on the wing region including the coalescence boundary, and on dislocated GaN (after Ref. 142).

because these defects induce an enhancement of the tunnel-assisted transport mechanism.¹⁵⁰

On the other hand, the spectral response shows a sharper cut-off in the case of devices on ELOG wings, covering or not covering the coalescence boundary, as shown in Figure 12.32. All these results are consistent with the observations in Schottky photodiodes on ELOG GaN.¹⁰¹

12.6.6 GaN-Based Avalanche Photodiodes

Avalanche photodiodes (APDs) present the advantages of high-speed, high-sensitivity, and large optical gain. They consist of a reverse biased p-n junction that is operated at voltages close to the breakdown.⁴ Photogenerated carriers in the SCR travel at their saturation velocity, due to the intense electric field, and may produce secondary electron–hole pairs by ionizing collisions with the lattice. These new electrons and holes again drift in opposite directions, and all or some of them may produce new carriers. This process is known as *impact ionization*, and leads to carrier multiplication and gain.

Calculations of the impact ionization parameters for electrons and holes in GaN^{151,152} indicate that the fields required to achieve multiplication are very high. Furthermore, because the impact ionization coefficients of electrons

and holes are predicted to be very similar, negative implications for the noise performance of GaN-based APD devices are expected. Finally, the high density of defects in this material prevents achieving homogeneous multiplication over the entire active area of the device.

GaN p-n junctions have been operated in the limit of breakdown (42–43 V) and a certain optical gain has been observed.¹⁵³ However, due to the high density of defects, breakdown is not homogeneous, as demonstrated by the appearance of bright spots of blue-light emission.

Ruden¹⁵⁴ proposed a hybrid III-nitride/Si APD structure that should be able to combine the visible-blind properties of AlGaN and the favorable impact ionization properties of Si. Light would be absorbed in the direct, wide-bandgap material and multiplication would take place in the Si region. This device could operate with a bias voltage of about 10 V.

12.7 PHOTOTRANSISTORS

The phototransistor is a photodetector which provides internal gain, and is therefore attractive for a number of applications. GaN bipolar and field effect phototransistors have been reported.^{155,156}

12.7.1 Bipolar Phototransistors

In a bipolar phototransistor, the reverse-biased base-collector junction operates as a p-n junction photodiode, and its photocurrent is amplified by transistor action. In the most common configuration, the base contact is not connected (floating-base operation).

Yang and colleagues¹⁵⁵ reported the fabrication of a GaN(n)/GaN(p)/GaN(i)/Al_{0.2}Ga_{0.8}N(n) heterojunction bipolar phototransistor. The electrical contacts were made to collector and emitter and the base was left floating. The UV light enters through the substrate (sapphire), travels through the *n*-Al_{0.2}Ga_{0.8}N layer, and is absorbed in the *i*-GaN layer. The photogenerated electron–hole pairs are separated by the field in the *i*-region, so that electrons and holes drift to the collector and to the base, respectively. The hole accumulation in the floating base increases electron injection from the emitter and results in a current gain. A gain in excess of 10⁵ has been demonstrated.¹⁵⁵

GaN-based bipolar phototransistors were found to present a sublinear behavior with optical power and persistent photoconductivity (PPC) similar to GaN photoconductors. Holes in the base should recombine with electrons injected from the emitter. However, holes are trapped in defects which reduce the recombination rate, inducing persistent effects. Yang and coworkers¹⁵⁵ realized that recombination is enhanced by biasing the detector to punch through and force the holes into the emitter. Thus, a voltage pulse is used as an electrical “reset.”

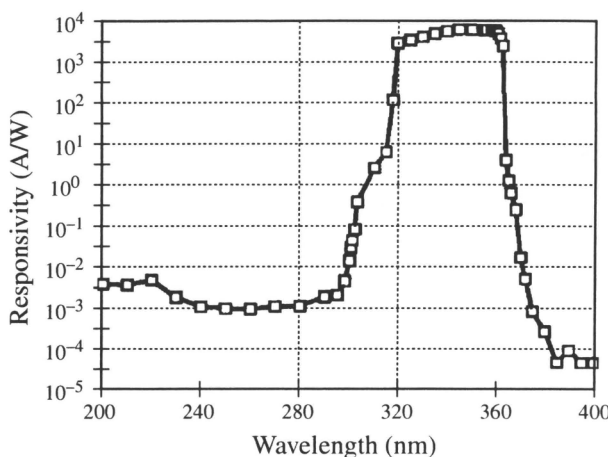


Figure 12.33 Spectral response of a GaN/AlGaN phototransistor (after Ref. 155).

To avoid persistent effects, the photodetector response is obtained under quenching-measuring cycles in which the device is subject to a 7 to 10 V “reset” pulse, and then biased at 3 to 4 V to measure photocurrent. In this scheme, the responsivity still decreases with optical power, and the gain is highly frequency-dependent, so that the gain-bandwidth product remains constant. For a frequency of 10 Hz, the spectral response of the device is shown in Figure 12.33. An excellent UV/visible contrast of eight orders of magnitude is obtained.¹⁵⁵

12.7.2 Field Effect Phototransistors

n-AlGaN/*n*-GaN/*i*-GaN heterostructure field effect transistors have also been characterized as UV photodetectors,¹⁵⁶ illuminating through the substrate (sapphire). The photogenerated holes move toward the *i*-GaN/sapphire interface, whereas the photogenerated electrons move toward the channel, where they are quickly driven into the drain by the intense electric field. These devices showed responsivities as high as 3000 A/W, a sharp cut-off, and a time response of about 0.2 ms.

12.8 CONCLUSIONS

The development of visible-blind UV photodetectors is being pushed by a number of applications, such as UV astronomy, ozone layer monitoring, engine control, missile plume detection, flame sensors, or secure space-to-space communications. With these purposes in view, Al_xGa_{1-x}N

photoconductors, Schottky photodiodes, metal-semiconductor-metal photodiodes, p-n and p-i-n junction photodetectors, and phototransistors have been recently developed.

$\text{Al}_x\text{Ga}_{1-x}\text{N}$ photoconductors present high internal gain at room temperature (~ 100 for $P_{opt} = 1 \text{ W/m}^2$). However, this gain is associated with a sublinear behavior with incident power, poor UV/visible contrast, and persistent photoconductivity effects. These drawbacks make photoconductors unsuitable for most applications. Both linearity and visible rejection can be considerably improved by using a lock-in detection system, but in this configuration photoconductors lose all their advantages, because responsivity is much reduced and the measuring system becomes more complex and expensive.

Schottky photodiode present a flat responsivity for excitation above the bandgap, independent of incident power and temperature, and show a sharp cut-off with a visible rejection of 10^3 . Their time response is RC -limited, with minimum time constants in the nanosecond range. These devices have proved to be suitable for environmental applications and UV-photodetector arrays.

Metal-semiconductor-metal photodiodes with very low dark currents have been fabricated. These devices are linear with optical power and present a UV/visible contrast of 10^4 . Provided their large bandwidth and low noise, these devices can be a good choice for visible-blind communications. Moreover, $\text{Al}_x\text{Ga}_{1-x}\text{N}$ MSM photodiodes could be easily integrated with III-nitride-based field effect transistors to fabricate optical receivers.

p-n and p-i-n junction photodiodes are linear with optical power and can present a visible rejection of 10^4 . However, their time response is usually limited by the behavior of Mg-related centers, which can also deteriorate the spectral response. The minimum cut-off wavelength of these devices is limited by the difficulty to achieve *p*-type $\text{Al}_x\text{Ga}_{1-x}\text{N}$ with high Al content. Although published results are promising, progress in *p*-type doping is required to improve the device performance and reliability.

Phototransistors combine high gain with a UV/visible contrast of 10^8 . Although their poor bandwidth makes them unsuitable for high-speed operation, these devices are promising for applications requiring good spectral resolution.

In summary, current results confirm $\text{Al}_x\text{Ga}_{1-x}\text{N}$ alloys as the best semiconductor choice for UV photodetection. However, device performance is still limited by the high density of defects in state-of-the-art heteroepitaxial layers. Therefore, further improvements are expected from progress in III-nitride growth and technology, as already obtained with epitaxial lateral overgrown material.

Acknowledgments

Thanks are due to Dr. B. Beaumont, Prof. P. Gibart, and Prof. M. Razeghi for technical support and encouragement. Support by EU Program Environment and Climate, Project ALDUV ENV4-CT97-0539 is acknowledged.

References

1. R. Koller, *Ultraviolet radiation* (Wiley & Sons, New York, 1965).
2. K. L. Coulson, *Solar and Terrestrial Radiation* (Academic Press, New York, 1975).
3. C. Bruehl and P. Crutzen, *Geophys. Res. Lett.*, **16**, 703 (1989).
4. P. Bhattacharya, *Semiconductor Optoelectronic Devices* (Prentice Hall, New Jersey, 1994).
5. F. Omnes, N. Marenco, B. Beaumont, Ph. de Mierry, E. Monroy, F. Calle, and E. Muñoz, *J. Appl. Phys.*, **86**, 5286 (1999).
6. S. M. Sze, *Physics of Semiconductor Devices* (Wiley, New York, 1981).
7. A. Rogalski, *Infrared Photon Detectors* (SPIE Optical Engineering Press, Washington, 1995).
8. A. Van der Ziel, *IEEE Proc.*, **58**, 8 (1970).
9. F. N. Hooge, *Phys. Lett.*, **29A**, 139 (1969).
10. J. I. Pankove and J. E. Berkeyheiser, *J. Appl. Phys.*, **45**, 3892 (1974).
11. B. W. Lim, Q. C. Chen, J. Y. Yang, and M. A. Khan, *Appl. Phys. Lett.*, **68**, 3761 (1996).
12. F. Binet, J. Y. Duboz, E. Rosencher, F. Scholz, and V. Härle, *Appl. Phys. Lett.*, **69**, 1202 (1996).
13. B. Shen, K. Yang, L. Zhan, Z. Chen, Y. Zhou, P. Chen, R. Zhan, Z. Huang, H. Zhou, and Y. Zheng, *Jpn. J. Appl. Phys.*, **38**, 767 (1999).
14. E. Muñoz, E. Monroy, J. A. Garrido, I. Izpura, F. J. Sánchez, M. A. Sánchez-García, E. Calleja, B. Beaumont, and P. Gibart, *Appl. Phys. Lett.*, **71**, 870 (1997).
15. E. Monroy, F. Calle, J. A. Garrido, P. Youinou, E. Muñoz, F. Omnes, B. Beaumont, and P. Gibart, *Semicond. Sci. Technol.*, **14**, 685 (1999).
16. P. Kung, X. Zhang, D. Walker, A. Saxler, J. Piotrowsky, A. Rogalski, and M. Razeghi, *Appl. Phys. Lett.*, **67**, 3792 (1995).
17. L. B. Flannery, I. Harrison, D. E. Lacklison, R. I. Dykeman, T. S. Chen, and C. T. Foxon, *Mat. Sci. Eng. B*, **50**, 307 (1997).
18. D. Walker, X. Zhan, A. Saxler, P. Kung, J. Xu, and M. Razeghi, *Appl. Phys. Lett.*, **70**, 949 (1997).
19. E. Monroy, F. Calle, E. Muñoz, F. Omnes, B. Beaumont, and P. Gibart, *J. Electron. Mat.*, **28**, 240 (1999).
20. J. Miragliotta and D. K. Wickenden, *Appl. Phys. Lett.*, **69**, 2095 (1996).
21. C. H. Qiu and J. I. Pankove, *Appl. Phys. Lett.*, **70**, 1983 (1997).
22. E. Monroy, J. A. Garrido, E. Muñoz, I. Izpura, F. J. Sánchez, M. A. Sánchez-García, E. Calleja, B. Beaumont, and P. Gibart, *MRS Internet J. Nitride Semicond. Res.*, **2**, art. 12 (1997).
23. K. S. Stevens, M. Kinniburgh, and R. Beresford, *Appl. Phys. Lett.*, **66**, 3518 (1995).
24. A. Y. Polyakov, N. B. Smirnov, A. V. Govorkov, and J. M. Redwing, *Solid-State Electron.*, **42**, 831 (1998).
25. M. T. Hirsch, J. A. Wolk, W. Walukiewicz, and E. E. Haller, *Appl. Phys. Lett.*, **71**, 1098 (1997).
26. C. H. Qiu, W. Melton, M. W. Leksono, J. I. Pankove, B. P. Keller, and S. P. Den Baars, *Appl. Phys. Lett.*, **69**, 1282 (1996).
27. G. Beardie, W. S. Rabinovich, A. E. Wickenden, D. D. Koleske, S. C. Binari, and J. A. Freitas, Jr., *Appl. Phys. Lett.*, **71**, 1092 (1997).
28. J. Z. Li, J. Y. Lin, H. X. Jiang, A. Salvador, A. Botchkarev, and H. Morkoç, *Appl. Phys. Lett.*, **69**, 1474 (1996).

29. C. Johnson, J. Y. Lin, H. X. Jiang, M. A. Khan, and C. J. Sun, *Appl. Phys. Lett.*, **68**, 1808 (1996).
30. H. M. Chen, Y. F. Chen, M. C. Lee, and M. S. Feng, *J. Appl. Phys.*, **82**, 899 (1997).
31. C. V. Reddy, K. Balakrishnan, H. Okumura, and S. Yoshida, *Appl. Phys. Lett.*, **73**, 244 (1998).
32. O. P. Seifert, O. Kirfel, M. Munzel, M. T. Hirsch, J. Parisi, M. Kelly, O. Ambacher, and M. Stutzman, *MRS Internet J. Nitride Semicond. Res.*, **4S1**, G5.5 (1999).
33. A. Van der Ziel, *Fluctuation Phenomena in Semiconductors* (Butterworths, Londres, 1959).
34. D. Long, *Infrared Phys.*, **7**, 169 (1967).
35. F. Binet, J. Y. Duboz, E. Rosencher, F. Scholz, and V. Härle, *Phys. Rev. B*, **54**, 8116 (1996).
36. J. A. Garrido, E. Monroy, I. Izpura, and E. Muñoz, *Semicond. Sci. Technol.*, **13**, 563 (1998).
37. M. Razeghi and A. Rogalsky, *J. Appl. Phys.*, **79**, 7433 (1996).
38. J. Salzman, C. Uzan-Saguy, B. Meyer, and R. Kalish, *Appl. Phys. Lett.*, **76**, 1431 (2000).
39. J. P. Vilcot, J. L. Vaterkowski, D. Decoster, and M. Constant, *Electron. Lett.*, **20**, 86 (1984).
40. D. Pascal, F. Hobar-Bourdeboss, S. Laval, C. Bru, J. P. Vilcot, D. Decoster, R. Fauquemberge, and M. Constant, *Ann. Télécommun.*, **40**, n 3-4 (1985).
41. J. W. Orton, B. J. Goldsmith, J. A. Chapman, and M. J. Powell, *J. Appl. Phys.*, **53**, 1602 (1982).
42. R. L. Petritz, *Phys. Rev.*, **104**, 1508 (1956).
43. T. Figielksi, *Solid-State Electron.*, **21**, 1403 (1978).
44. C. H. Qiu, C. Hoggatt, W. Melton, M. W. Leksono, and J. I. Pankove, *Appl. Phys. Lett.*, **66**, 2712 (1995).
45. A. Y. Polyakov, N. B. Smirnov, A. V. Govorkov, M. G. Mil'vidskii, J. M. Redwing, M. Shin, M. Skowronski, D. W. Greve, and R. G. Wilson, *Solid-State Electron.*, **42**, 627 (1998).
46. A. Y. Polyakov, N. B. Smirnov, A. S. Usikov, A. V. Govorkov, and B. Pushniy, *Solid-State Electron.*, **42**, 1959 (1998).
47. J. Z. Li, J. Y. Lin, H. X. Jiang, M. A. Khan, and Q. Chen, *J. Appl. Phys.*, **82**, 1227 (1997).
48. J. Z. Li, J. Y. Lin, H. X. Jiang, and M. A. Khan, *Appl. Phys. Lett.*, **72**, 2868 (1998).
49. A. V. Buyanov, J. P. Bergman, J. A. Sandberg, B. E. Sernelius, P. O. Holtz, J. Dalfors, B. Monemar, H. Amano, and I. Akasaki, *J. Crystal Growth*, **189/190**, 753 (1998).
50. J. Y. Lin, A. D. Dissanayake, G. Brown, and H. X. Jiang, *Phys. Rev. B*, **42**, 5855 (1990).
51. J. Y. Lin and H. X. Jiang, *Phys. Rev. B*, **41**, 5178 (1990).
52. D. V. Lang and R. A. Logan, *Phys. Rev. Lett.*, **39**, 635 (1977).
53. H. J. Queisser, *Phys. Rev. Lett.*, **54**, 234 (1985).
54. F. L. Gouin, Z.-M. Li, J. P. Noad, S. P. AcAlister, W. R. McKinnon, and C. M. Hurd, *IEEE Trans. Electron Dev.*, **39**, 297 (1992).
55. R. G. Decorbry, R. I. McDonald, M. Beaudoin, T. Pinnington, T. Tiedje, and F. Gouin, *J. Electron. Mat.*, **26**, L25 (1997).
56. D. M. Collins, D. E. Mars, B. Fisher, and C. Kocot, *J. Appl. Phys.*, **54**, 858 (1983).
57. P. Boguslawski and J. Bernholc, *Phys. Rev. B*, **56**, 9496 (1997).
58. C. H. Park and D. J. Chadi, *Phys. Rev. B*, **55**, 12995 (1997).
59. J. Neugebauer and C. G. Van de Walle, *Appl. Phys. Lett.*, **69**, 503 (1996).
60. C. G. Van de Walle, *Phys. Rev. B*, **57**, R2033 (1998).
61. C. Wetzel, T. Suski, J. W. Ager, E. R. Weber, E. E. Haller, S. Fisher, B. K. Meyer, R. J. Molnar, and P. Perlin, *Phys. Rev. Lett.*, **78**, 3923 (1997).
62. C. Skiebzewski, T. Suski, M. Leszczynski, M. Shin, M. Skowronski, M. D. Bremser, and R. F. Davis, *Appl. Phys. Lett.*, **74**, 3833 (1999).
63. I.-H. Lee, J. J. Lee, P. Kung, F. J. Sánchez, and M. Razeghi, *Appl. Phys. Lett.*, **74**, 102 (1999).
64. A. Dissanayake, M. Elahi, H. X. Jiang, and J. Y. Lin, *Phys. Rev. B*, **45**, 13996 (1992).

65. Z. C. Huang, D. B. Mott, P. K. Shu, R. Zhang, J. C. Chen, and C. K. Wickenden, *Appl. Phys. Lett.*, **82**, 2707 (1997).
66. V. A. Joskina, J. C. Roberts, F. G. McIntosh, S. M. Bedair, E. L. Piner, and M. K. Behbehani, *Appl. Phys. Lett.*, **71**, 234 (1997).
67. J. Neugebauer and C. B. Van de Walle, *Phys. Rev. Lett.*, **75**, 4452 (1995).
68. C. G. Van de Walle, C. Stampfl, J. Neugebauer, M. D. McCluskey, and N. M. Johnson, *MRS Internet J. Nitride Semicond. Res.*, **4S1**, G10.4 (1999).
69. M. D. McCluskey, N. M. Johnson, C. G. Van de Walle, D. P. Bour, M. Kneissl, and W. Walukiewicz, *Phys. Rev. Lett.*, **80**, 4008 (1998).
70. P. J. Hansen, Y. E. Strausser, A. N. Erickson, E. J. Tarsa, P. Kozodoy, E. G. Brazel, J. P. Ibbetson, U. Mishra, V. Narayananamurti, S. P. DenBaars, and J. S. Speck, *Appl. Phys. Lett.*, **72**, 2247 (1998).
71. V. M. Bermudez, T. M. Jung, K. Doverspike, and A. E. Wickenden, *J. Appl. Phys.*, **79**, 101 (1996).
72. V. M. Bermudez, *J. Appl. Phys.*, **80**, 1190 (1996).
73. Z. Z. Bandić, P. M. Bridger, E. C. Piquette, and T. C. McGill, *Appl. Phys. Lett.*, **72**, 3166 (1998).
74. M. Misra, D. Doppalapudi, A. V. Sampath, T. D. Moustakas, and P. H. McDonald, *MRS Internet J. Nitride Semicond. Res.*, **4S1**, G7.8 (1999).
75. N. V. D'yakonova, M. E. Levinstein, S. Contreras, W. Knap, B. Beaumont, and P. Gibart, *Semicond.*, **32**, 257 (1998).
76. M. A. Khan, J. N. Kuznia, D. T. Olson, J. M. Van Hove, M. Blasingame, and L. F. Reitz, *Appl. Phys. Lett.*, **60**, 2917 (1992).
77. J. I. Pankove, J. T. Torvik, C. H. Qiu, I. Grzegory, S. Porowski, P. Quigley, and B. Martin, *Appl. Phys. Lett.*, **74**, 416 (1999).
78. G. M. Smith, J. M. Redwing, R. P. Vaudo, E. M. Ross, J. S. Flynn, and V. M. Phanse, *Appl. Phys. Lett.*, **75**, 25 (1999).
79. Y. Morimoto and S. Ushio, *Jpn. J. Appl. Phys.*, **13**, 365 (1974).
80. M. A. Khan, J. N. Kuznia, D. T. Olson, M. Blasingame, and A. R. Bhattachari, *Appl. Phys. Lett.*, **63**, 2455 (1993).
81. J. M. Mooney and J. Silverman, *IEEE Trans. Electron Dev.*, **ED-32**, 33 (1984).
82. V. E. Vickers, *Appl. Opt.*, **10**, 2190 (1971).
83. V. L. Dalal, *J. Appl. Phys.*, **42**, 2274 (1971).
84. R. H. Fowler, *Phys. Rev.*, **38**, 45 (1931).
85. F. Binet, J. Y. Duboz, N. Laurent, E. Rosenthaler, O. Briot, and R. L. Aulombard, *J. Appl. Phys.*, **81**, 6449 (1997).
86. X. Zhang, P. Kung, D. Walker, J. Piotrowski, A. Rogalski, A. Saxler, and M. Razeghi, *Appl. Phys. Lett.*, **67**, 2028 (1995).
87. Q. Chen, J. W. Yang, A. Osinsky, S. Gangopadhyay, B. Lim, M. Z. Anwar, M. A. Khan, D. Kuksenkov, and H. Temkin, *Appl. Phys. Lett.*, **70**, 2277 (1997).
88. A. Osinsky, S. Gangopadhyay, B. Lim, M. Z. Anwar, M. A. Khan, D. Kuksenkov, and H. Temkin, *Appl. Phys. Lett.*, **72**, 742 (1998).
89. E. Monroy, F. Calle, C. Angulo, P. Vila, A. Sanz, J. A. Garrido, E. Calleja, E. Muñoz, S. Haffouz, B. Beaumont, F. Omnes, and P. Gibart, *Appl. Opt.*, **37**, 5058 (1998).
90. E. Monroy, F. Calle, E. Muñoz, F. Omnes, P. Gibart, and J. A. Muñoz, *Appl. Phys. Lett.*, **73**, 2146 (1998).
91. E. Monroy, F. Calle, E. Muñoz, F. Omnes, B. Beaumont, P. Gibart, J. A. Muñoz, and F. Cussó, *MRS Internet J. Nitride Semicond. Res.*, **3**, art. 9 (1998).
92. E. Muñoz, E. Monroy, F. Calle, M. A. Sánchez, E. Calleja, F. Omnes, P. Gibart, F. Jaque, and I. Aguirre de Cárcer, *SPIE Proc.*, **3629**, 200 (1999).
93. A. Osinsky, S. Gangopadhyay, B. Lim, M. Z. Anwar, M. A. Khan, D. Kuksenkov, H. Temkin, I. K. Shmagin, Y. C. Chang, J. F. Muth, and R. M. Kolbas, *Appl. Phys. Lett.*, **72**, 551 (1998).
94. G. Simin, M. A. Khan, J. W. Yang, A. Lunev, V. Adivarahan, N. Pala, M. Shur, R. Gasca, "Low dark current transparent Schottky barrier UV detectors", Proc. 3rd International Conference on Nitride Semicond. (Montpellier, 1999).

95. N. G. Weimann, L. F. Eastman, D. Doppalapudi, H. M. Ng, and T. D. Moustakas, *J. Appl. Phys.*, **83**, 3656 (1998).
96. C.-Y. Hwang, M. J. Schurman, W. E. Mayo, Y.-C. Lu, R. A. Stall, and T. Salagaj, *J. Electron. Mat.*, **26**, 243 (1997).
97. A. Usui, H. Sunakawa, A. Sakai, and A. Yamaguchi, *Jpn. J. Appl. Phys.*, **36**, L899 (1997).
98. O. H. Nam, M. D. Bremser, T. Zheleva, and R. F. Davis, *Appl. Phys. Lett.*, **71**, 2638 (1997).
99. K. Linthicum, T. Gehrke, D. Thomson, E. Carlson, P. Rajagopal, T. Smith, D. Bachelor, and R. Davis, *Appl. Phys. Lett.*, **75**, 196 (1999).
100. B. Beaumont, M. Vaille, G. Nataf, A. Bouillé, J. C. Guillaume, P. Vénnègues, S. Haffouz, and P. Gibart, *MRS Internet J. Nitride Semicond. Res.*, **3**, art. 20 (1998).
101. E. Monroy, F. Calle, E. Muñoz, B. Beaumont, F. Omnes, and P. Gibart, *Electron. Lett.*, **35**, 1488 (1999).
102. A. F. McKinley and B. L. Diffey, *CIE Journal*, **6**, 17 (1987).
103. F. R. De Gruji and J.C. Van der Leun, *Health Phys.*, **67**, 314 (1994).
104. R. B. Setlow, *Proc. Natl. Acad. Sci., USA*, **71**, 3363 (1974).
105. L. W. Jones and B. Kok, *Plant Physiol.*, **41**, 1037 (1966).
106. M. Morys and D. Berger, *SPIE Proc.*, **2049**, 152 (1993).
107. E. Muñoz, E. Monroy, F. Calle, F. Omnes, and P. Gibart, *J. Geophys. Res.*, **105**, 4865 (2000).
108. B. W. Lim, S. Gangopadhyay, J. W. Yang, A. Osinsky, Q. Chen, M. Z. Anwar, and M. A. Khan, *Electron. Lett.*, **33**, 633 (1997).
109. M. Ito, O. Wada, K. Nakai, and T. Sakurai, *IEEE Electron Device Lett.*, **EDL-5**, 531 (1984).
110. S. M. Sze, D. J. Coleman, Jr., and A. Loya, *Solid-State Electron.*, **14**, 1209 (1971).
111. Y. C. Lim and R. A. Moore, *IEEE Trans. Electron Dev.*, **ED-15**, 173 (1968).
112. L. W. Cahill, *SPIE Proc.*, **3629**, 453 (1999).
113. L. W. Cahill, *SPIE Proc.*, **2999**, 78 (1997).
114. E. Monroy, F. Calle, E. Muñoz, and F. Omnes, *Physica Status Solidi A*, **176**, 157 (1999).
115. J. C. Carrano, T. Li, P. A. Grudowski, C. J. Eiting, R. D. Dupuis, and J. C. Campbell, *J. Appl. Phys.*, **83**, 6148 (1998).
116. E. Monroy, F. Calle, E. Muñoz, and F. Omnes, *Appl. Phys. Lett.*, **74**, 3401 (1999).
117. E. Monroy, F. Calle, E. Muñoz, F. Omnes, B. Beaumont, and P. Gibart, "Visible-blind ultraviolet photodetectors based on $\text{Al}_x\text{Ga}_{1-x}\text{N}$ alloys", Proc. 26th International Symp. on Compound Semicon. (August, 1999).
118. D. Walker, E. Monroy, P. Kung, J. Wu, M. Hammilton, F. J. Sánchez, J. Diaz, and M. Razeghi, *Appl. Phys. Lett.*, **74**, 762 (1999).
119. J. C. Carrano, P. A. Grudowski, C. J. Eiting, R. D. Dupuis, and J. C. Campbell, *Appl. Phys. Lett.*, **70**, 1992 (1997).
120. S. F. Soares, *Jpn. J. Appl. Phys.*, **31**, 210 (1992).
121. M. Klingenstein and J. Khul, *Solid-State Electron.*, **37**, 333 (1994).
122. J. Burn and L. F. Eastman, *IEEE Photonics Technol. Lett.*, **8**, 113 (1996).
123. J. C. Carrano, T. Li, P. A. Grudowski, C. J. Eiting, R. D. Dupuis, and J. C. Campbell, *Electron. Lett.*, **33**, 1980 (1997).
124. J. C. Carrano, T. Li, C. J. Eiting, R. D. Dupuis, and J. C. Campbell, *J. Electron. Mat.*, **28**, 325 (1999).
125. R. P. Joshi, A. N. Dharamsi, and J. McAdoo, *Appl. Phys. Lett.*, **64**, 3611 (1994).
126. R. P. Joshi, *J. Appl. Phys.*, **76**, 4434 (1994).
127. E. Monroy, F. Calle, E. Muñoz, F. Omnes, and P. Gibart, *Electron. Lett.*, **35**, 240 (1999).
128. P. Kung, D. Walker, P. Sandvik, M. Hamilton, J. Diaz, I.-H. Lee, and M. Razeghi, *SPIE Proc.*, **3629**, 223 (1999).
129. Q. Chen, M. A. Khan, C. J. Sun, and J. W. Yang, *Electron. Lett.*, **31** (1995).
130. E. Monroy, E. Muñoz, F. J. Sánchez, F. Calle, E. Calleja, B. Beaumont, P. Gibart, J. A. Muñoz, and F. Cussó, *Semicod. Sci. Technol.*, **13**, 1024 (1998).
131. A. Osinsky, S. Gangopadhyay, R. Gaska, B. Williams, M. A. Khan, D. Kuksenkov, and H. Temkin, *Appl. Phys. Lett.*, **71**, 2334 (1997).

132. J. M. Van Hove, R. Hickman, J. J. Klaassen, P. P. Chow, and P. P. Ruden, *Appl. Phys. Lett.*, **70**, 2282 (1997).
133. D. Walker, A. Saxler, P. Kung, X. Zhang, M. Hamilton, J. Diaz, and M. Razeghi, *Appl. Phys. Lett.*, **72**, 3303 (1998).
134. J. C. Carrano, T. Li, P.A. Grudowski, C. J. Eiting, D. Lambert, J. D. Schaub, R. D. Dupuis, and J. C. Campbell, *Electron. Lett.*, **34**, 692 (1998).
135. J. C. Carrano, T. Li, D. L. Brown, P. A. Grudowski, C. J. Eiting, R. D. Dupuis, and J. C. Campbell, *Electron. Lett.*, **34**, 1779 (1998).
136. G. Y. Xu, A. Salvador, W. Kim, Z. Fan, C. Lu, H. Tang, H. Morkoç, G. Smith, M. Estes, B. Goldenberg, W. Yang, and S. Krishnankutty, *Appl. Phys. Lett.*, **71**, 2154 (1997).
137. S. Krishnankutty, W. Yang, T. Nohava, and P. P. Ruden, *MRS Internet J. Nitride Semicond. Res.*, **3**, art. 7 (1998).
138. W. Yang, T. Nohava, S. Krishnankutty, R. Torreano, S. McPherson, and H. Marsh, *Appl. Phys. Lett.*, **73**, 1086 (1998).
139. J. D. Brown, Z. Yu, J. Matthews, S. Harney, J. Boney, J. F. Schetzina, J. D. Benson, K. W. Dang, C. Terril, T. Nohava, W. Yang, and S. Krishnankutty, *MRS Internet J. Nitride Semicond. Res.*, **4**, 9 (1999).
140. E. Monroy, M. Hamilton, D. Walker, P. Kung, F. J. Sánchez, and M. Razeghi, *Appl. Phys. Lett.*, **74**, 1171 (1999).
141. D. Walker, P. Kung, P. Sandvik, J. Wu, M. Hamilton, I.-H. Lee, J. Diaz, and M. Razeghi, *SPIE Proc.*, **3629**, 193 (1999).
142. G. Parish, S. Keller, P. Kozodoy, J. P. Ibbetson, H. Marchand, P. T. Fini, S. B. Fleischer, S. P. DenBaars, U. K. Mishra, and E. J. Tarsa, *Appl. Phys. Lett.*, **75**, 247 (1999).
143. D. L. Pulfrey and B. D. Nener, *Solid-State Electron.*, **42**, 1731 (1998).
144. P. Blood and J. W. Orton, "Electrical characterization of semiconductors: majority carriers and electron states," in *Techniques of Physics*, Vol. 14 (Academic Press, London, 1992).
145. I. Akasaki, H. Amano, M. Kito, and K. Hiramatsu, *J. Lumin.*, **48/49**, 666 (1991).
146. Y. Zohta, H. Kuroda, R. Nii, and S. Nakamura, *J. Cryst. Growth*, **189/190**, 816 (1998).
147. D. W. Kuksenkov, H. Tmkin, A. Osinsky, R. Gaska, and M. A. Khan, *J. Appl. Phys.*, **83**, 2142 (1998).
148. B. I. Shklovskii, *Solid-State Commun.*, **33**, 273 (1980).
149. T. L. Tansley and R. J. Egan, *Physica B*, **185**, 190 (1993).
150. L. S. Yu, Q. Z. Liu, Q. J. Xing, D. J. Qiao, S. S. Lau, and J. Redwing, *J. Appl. Phys.*, **84**, 2099 (1998).
151. J. Kolnik, I. H. Oguzman, K. F. Brennan, R. Wang, P. P. Ruden, and Y. Wang, *J. Appl. Phys.*, **78**, 1033 (1995).
152. I. H. Oguzman, E. Bellotti, K. F. Brennan, J. Kolnik, R. Wang, and P. P. Ruden, *J. Appl. Phys.*, **81**, 7827 (1997).
153. A. Osinsky, M. S. Shur, R. Gaska, and Q. Chen, *Electron. Lett.*, **34**, 691 (1998).
154. P. P. Ruden, *SPIE Proc.*, **3629**, 174 (1999).
155. W. Yang, T. Nohava, S. Krishnankutty, R. Torreano, S. Mcpherson, and H. Marsh, *Appl. Phys. Lett.*, **73**, 978 (1998).
156. M. A. Khan, M. S. Shur, Q. Chen, J. N. Kuznia, and C. J. Sun, *Electron. Lett.*, **31**, 398 (1998).